LAWRENCE
LIVERMORE
NATIONAL
LABORATORY

LLNL-JRNL-517791

Ocean Salinities Reveal Strong Global Water Cycle Intensification during 1950-2000

P. J. Durack, S. E. Wijffels, R. J. Matear

December 2, 2011

Science

Ocean Salinities Reveal Strong Global Water Cycle Intensification during 1950-2000

Paul J. Durack[1,2,3,4], Susan E. Wijffels[1,3] and Richard J. Matear[1]

[1]Centre for Australian Weather and Climate Research, CSIRO Marine and Atmospheric Research, GPO Box 1538, Hobart, Tasmania 7001, Australia

[2]Institute for Marine and Antarctic Studies, University of Tasmania, Private Bag 129, Hobart, Tasmania 7001, Australia

[3]Wealth from Oceans National Research Flagship, CSIRO, GPO Box 1538, Hobart, Tasmania 7001, Australia

[4]Program for Climate Model Diagnosis and Intercomparison, Lawrence Livermore National Laboratory, Mail Code L-103, 7000 East Avenue, Livermore, California 94550, USA.

Abstract: 116 words; Body text: 2233 words (excluding introductory paragraph)
Resubmitted to Science 17th November 2011

Summary sentence: New estimates of water cycle intensification inferred from observed ocean salinity changes suggest a 4% intensification has occurred from 1950 to 2000, twice the response projected by current generation global climate models.

Abstract: Fundamental thermodynamics and climate models suggest dry regions will become drier and wet regions will become wetter in response to warming. Efforts to detect this long-term response in sparse surface observations of rainfall and evaporation remain ambiguous. We show ocean salinity patterns express a clearly identifiable fingerprint of an intensifying water cycle. Our 50-year observed global surface salinity changes, combined with changes from global climate models, present robust evidence of an intensified global water cycle at a rate of 8±5% per degree of surface warming. This rate is double the response projected by current generation climate models and suggests a substantial (16-24%) intensification of the global water cycle will occur in a future 2-3° warmer world.

Introductory paragraph: A warming of the global surface and lower atmosphere is expected to strengthen the water cycle (*1-3*) largely driven by the ability of warmer air to hold and to redistribute more moisture. This intensification is expressed as an enhancement in the patterns of surface water fluxes (evaporation and rainfall [E-P]) and as a consequence, ocean surface salinity patterns. According to the Clausius-Clapeyron (CC) relation and assuming a fixed relative humidity, we expect a ~7% increase in atmospheric moisture content for every degree of warming of the Earth's lower troposphere (*2*). Of greatest importance to society, and the focus of this work, is the strength of the regional pattern of evaporation and precipitation (E-P), which in climate models scales approximately with CC, while global precipitation changes more slowly at a rate of 2-3% $°C^{-1}$ (*2, 4*).

An intensification of existing patterns of global mean surface evaporation and precipitation (E-P) is found along with enhancements to extreme events such as droughts and floods (*1, 5*) in available 21st century climate projections, forced by anthropogenic greenhouse gases (GHG) from the Coupled Model Intercomparison Project Phase 3 (CMIP3 (*6*)). This has been labelled the "rich get richer" mechanism, where wet areas (compared to the global mean) get wetter and dry regions drier (*7*). There is, however, little consistency in the seasonal changes provided by model projections, and poor agreement when compared to regional observational estimates (*8*). Additionally, atmospheric aerosols included in these projections can regionally counteract the GHG-driven warming, and act to suppress the local water cycle through dynamical changes (*9, 10*).

Given the above broad-scale model responses and the CC relationship, an intensification of ~4% in the global water cycle (E-P) is expected to already have occurred in response to the observed 0.5°C warming of the Earth's surface over the past 50-years (*11*). However, obtaining a global view of historical long-term rainfall pattern changes is made difficult due to the spatially sparse and short observational record. Long, high-quality land-based records are few and northern hemisphere biased (*12*). Direct high quality long-term rainfall estimates over oceans (which comprise 71% of the global surface area and receive over 80% of global rainfall (*13*); Fig. S1) are very scarce, with most global observational products dependent on data contributions from satellites, themselves sensitive to error (*14, 15*). Additionally, due to the short temporal coverage (~15-30 years) by satellite missions, trends are likely affected by natural decadal modes of variability, and may dominate much of the measured changes (*3*). This challenge is exacerbated by the spatially and temporally sporadic nature of rainfall, making the derivation of broad-scale averages of small multidecadal changes from a sparse network of observing stations error-prone (*16*). These difficulties are evident in the differing signs of long-term trends between reconstructed rainfall datasets (*17, 18*). Discrepancies among air-sea evaporative flux products (*19*) undermine their use in resolving long-term water cycle changes. As a result, we do not yet have a definitive view on whether the Earth's water cycle has intensified over the past several decades from atmospheric observing networks (*12, 20*).

It has long been noted that the climatological mean sea surface salinity (SSS) spatial pattern is highly correlated with the long-term mean E-P spatial pattern (*21*) (Fig. 1A, D), reflecting the balance between ocean advection/mixing processes and E-P forcing at the ocean surface (*21-23*). Several studies of multidecadal SSS changes reveal a clear pattern where increasing salinities are found in the evaporation dominated mid-latitudes and decreasing salinities in the rainfall dominated regions such as the tropical atmospheric convergence zones and polar regions (*22, 24-27*). These previous studies have used optimally averaged pentadal historical ocean data (*24*) or the difference between pre-2000 and post-2000 climatologies (*27*), the latter period being strongly supported by the modern baseline provided by the Argo Programme (*28*) to investigate long-term salinity changes in the global ocean. Using a direct local fit of trends to historical and Argo data simultaneously (*25*), we map the multidecadal linear SSS trends back to 1950 (Fig. 1D, G). Over the last 50-years SSS changes reflect an intensification of the mean SSS patterns. This strong and coherent relationship is expressed through the high spatial pattern correlation coefficient (PC) of ~0.7 (Figure S2) between the mean SSS and independent estimates of long-term SSS change (*24, 25, 27*). Following the "rich get richer" mechanism (*7*), salty ocean regions (compared to the global mean) are getting saltier, while fresh regions are getting fresher. This robust intensification of the observed SSS pattern is qualitatively consistent with increased E-P if ocean mixing and circulation are largely unchanged.

[Figure 1 about here]

In trying to quantitatively relate SSS changes and E-P changes previous studies have made strong simplifying assumptions. One estimate of a global 3.7% E-P intensification from 1970s to 2005 (*27*) is based on the assumption of an unchanging ocean mixing and advection field, with the additional assumption that no salt or freshwater exchange has occurred over this time with the deep ocean below 100m. However, several studies have shown subsurface salinity changes have occurred during the 20^{th} century (*24, 25*), with many of the largest signals expressed at depths greater than 100m. Another study used subsurface salinity changes on isopycnals to deduce E-P changes at the surface density outcrops (*26*). This approach is error prone as broad-scale salinity changes on density surfaces can largely be explained by the subduction of broad-scale warming and not E-P changes alone (*25*). To avoid such strong assumptions and explore the use of SSS pattern changes as a water cycle diagnostic, we use the most comprehensive simulations available to date of the historical and future global climate - the CMIP3 simulations of the 20^{th} century (20C3M) and Special Report on Emissions Scenarios (SRES) 21^{st} century future projections (*6*). Within these simulations we investigate the relationship between SSS and E-P pattern changes. These simulations capture the full range of complex dynamical changes in response to greenhouse gas (GHG) forcing, which include: ocean surface (and subsurface) temperature changes, dynamical shifts to ocean and atmospheric circulation, upper ocean stratification changes as well as the regional effects of aerosols on water cycle operation.

To quantify and compare the strength of broad-scale SSS pattern intensification in both observations and CMIP3, zonal ocean basin (Pacific, Atlantic and Indian) averages were formed for both the mean SSS and its 50-year (1950-2000) linear trends. A linear regression is undertaken using the basin zonal averages of the climatological mean SSS (x-axis) anomaly against the SSS change pattern (y-axis; Fig. 1J). We define the resulting slope of this relationship as the pattern amplification (PA) and the correlation coefficient (R) as the pattern correlation (PC). A key advantage of this analysis is its insensitivity to the mean spatial climatological biases in model fields (*29*) when compared to observations, since the model change fields are compared to their own model climatology. We formed the PA and PC metrics for each model simulation and our observational analysis (Fig. S2 presents comparative global zonal mean analyses for available global SSS studies).

Analysis of trends in observed SSS indicates that from 1950 to 2000 the SSS PA is 8% with a PC of 0.7 (Fig. 1J). Similar to observations, many models show a high PC (~0.7-0.9) between the climatological mean SSS and the corresponding climatological mean E-P. However, most 20C3M model simulations show a weaker than observed spatial pattern correlation (PC) and pattern amplification (PA) between the 50-year SSS mean and SSS change patterns (Fig. 1D, G vs E, H & F, I), and do not uniformly provide a realistic simulation of observed surface mean SSS patterns or its change over 1950-2000 (Fig. 1D, G; Fig. S6, Table S2). Our examples of the simulations that most closely replicate the observed spatial change and mean patterns (Fig. 1E, H) and those that produce an almost inverse spatial change pattern (Fig. 1F, I) compared to the observed results (Fig. 1D, G), illustrate the range of responses found in CMIP3 (Fig. 1). Some models show similar numbers to those observed (Fig. 1E, H, K) while others have very low values of both PA and PC (Fig. 1F, I, L), indicating no clear SSS pattern amplification. Such discrepancies raise a key question: What controls this difference in the modelled SSS response and how is this related to water cycle changes?

[Figure 2 about here]

The PA and PC methodology can also be used when considering other variables, such as the surface water flux (E-P). CMIP3 simulations show a relationship between SSS PA and the E-P PA (Fig. 2B). This key result supports the use of SSS PA as a diagnostic of a changing water cycle, and also provides a relationship in which to consider the observed SSS PA for 1950-2000. The CMIP3 SSS patterns amplify at twice the rate of E-P patterns (Fig. 2B). The reason that E-P PA drives a stronger response in SSS PA for CMIP3 is not clearly understood, and requires further investigation, but the relationship between them is compelling.

When investigating water cycle changes, it is important to consider the coincident global surface warming, the natural framework of water cycle amplification. If expressed in a per degree warming context, such water cycle rate changes can then be directly compared to other studies, both oceanographic and atmospheric in their origins (Table S3, Figure S9).

For both the 20C3M and SRES CMIP3 simulations, we find a clear relationship between the rate of global average surface warming (ΔTa) and the rate of SSS PA and PC strength (Fig. 2A). 20C3M simulations in which the warming rate is low (generally those with comprehensive aerosol schemes; contrast diamonds and circles in Fig. S5; Table S1) feature low SSS PA, with spatial change patterns having only slight correspondence to the spatial mean pattern and consequently a low SSS PC (illustrated by the simulation in Fig. 1F, I, L). The stronger warming SRES simulations express a clearer and larger pattern amplification response (PC > 0.5) than most 20C3M simulations (Fig. 2A). The increase in PC with enhanced PA suggests a signal-to-noise process is operating, where in weakly warming simulations model internal variability dominates the change signal. A PC-weighted line of best fit through the 93 CMIP3 simulations suggests that SSS patterns intensify with warming at 8% °C^{-1} (Fig. 2A), which is half of our 1950-2000 observed rate (16% °C^{-1}; Fig. 2A). As expected, based on past analyses of CMIP3 (*2*), the E-P PA is also linearly related to surface warming rates (Fig. 2C) with the model line of best fit below CC (4.5% °C^{-1}). Also in agreement with many previous analyses (*1, 2*), total global average rainfall is linearly related to warming rates but with a distinctively weaker slope than surface water flux, near 3.1% °C^{-1} (Fig. 2D). The stronger SSS PA response to warming and tighter agreement among CMIP3 when compared to that for the E-P PA (Fig. 2A vs C) suggests that long-term SSS pattern changes provide a clearly identifiable, highly detectable and particularly sensitive measure of long-term water cycle changes. It is likely that ocean mixing and circulation act to integrate and smooth the temporal and spatial patchiness of E-P fluxes at the ocean surface and provide a smoothed SSS anomaly field, which facilitates detection of broad-scale, persistent changes.

To independently demonstrate the strong relationship between 50-year salinity change and an enhanced water cycle, the response of an ocean-only model to an idealised 5% E-P pattern increase was explored. We used a version of the MOM3 ocean model, forced with E-P fields obtained from the NCEP reanalysis. A linear trend in E-P was imposed to achieve a 5% increase over 50-years. The resulting spatial pattern of SSS change strongly mirrors the observed and CMIP3 ensemble mean patterns, but with smaller absolute magnitudes (Fig. 3A, C, D vs 3B). The salinity pattern amplification is expressed for surface and subsurface changes (Figs. S7 & S8; see supporting online material). Therefore in a global ocean-only model, spatial salinity patterns enhance in response to an intensified E-P. A similar spatial response to the observed changes are found in CMIP3 but only for the strongly warming 20C3M simulations (>0.5°C; Fig. 3D vs 3C). Those simulations with less than the observed warming over 1950-2000 often incorporate aerosol effects which act to reduce warming (contrast diamonds and circles in Fig. S5), and thus under predict the subsequent water cycle amplification as expressed in SSS changes.

[Figure 3 about here]

Despite their scatter, estimates from the CMIP3 ensemble show a weaker salinity pattern amplification per degree of warming (8% °C^{-1}; Fig. 2A) than has been observed (16% °C^{-1}; Fig. 2A). Using the modelled relationship between SSS PA and E-P PA from the CMIP3 ensemble (which shows that SSS PA increases at twice the rate of E-P PA (Fig. 2B)), and applying this relationship to our observed SSS PA estimate, we infer that over the past 50 years the global water cycle has amplified by 4%. Using the observed 0.5°C surface warming estimate (*11*), this inferred water flux amplification of 8% $°C^{-1}$, is close to that predicted by the CC relationship (~7% $°C^{-1}$). This rate of change is consistent with many other independent observational estimates (Table S3, Fig. S9) which all provide evidence that an observed global water cycle amplification has occurred. However, CMIP3 ensemble averages of E-P PA produce a rate well below this of 4.5% $°C^{-1}$ (Fig. 2C).

A change to freshwater availability in response to climate change poses a more significant risk to human societies and ecosystems than warming alone. Changes to the global water cycle and the corresponding redistribution of rainfall will affect food availability, stability, access and utilisation. We show that ocean salinity is a particularly sensitive marker of water cycle change which provides us with a salty ocean freshwater "gauge" from which to monitor over 71% of the Earth's surface. Using ocean observations we show the "rich get richer" mechanism is already operating, with fresh regions becoming fresher and salty regions saltier in response to observed warming. Our results support a water cycle intensification rate consistent with the CC relationship under fixed relative humidity. In a future greenhouse gas forced 2-3°C warmer world (*30*), this implies a 16-24% amplification of the global water cycle will occur, nearly double the CMIP3 response.

Acknowledgements This work has been undertaken as part of the Australian Climate Change Science Program, funded jointly by the Department of Climate Change and Energy Efficiency, the Bureau of Meteorology and CSIRO. P.J.D. was supported by a joint QMS-University of Tasmania Ph.D. scholarship in Quantitative Marine Science (QMS) with support from CSIRO's Wealth from Oceans Flagship. Additional support was provided under the auspices of the U.S. Department of Energy by Lawrence Livermore National Laboratory contract DE-AC52-07NA27344. We acknowledge the modelling groups, the Program for Climate Model Diagnosis and Intercomparison (PCMDI) and the WCRP's Working Group on Coupled Modelling (WGCM) for their roles in making available the WCRP CMIP3 multi-model data set. The authors would also like to thank numerous colleagues from CSIRO, the Centre for Australian Weather and Climate Research (CAWCR), and the University of Tasmania for valuable feedback and input into this project. The Centre for Australian Weather and Climate Research is a partnership between CSIRO and the Australian Bureau of Meteorology. The authors thank Drs. Julia Durack of the University of Tasmania, Stephen Griffies of the Geophysical Fluid Dynamics Laboratory (GFDL) and Robert Colman of CAWCR for helpful comments with early drafts of this manuscript.

Author Contributions P.J.D. conceived the study, completed the analysis and shared responsibility for writing the manuscript. S.E.W. assisted in the analysis and shared responsibility for writing the manuscript. R.J.M. undertook the idealised model simulations. All authors contributed to the final version of the manuscript.

Author Information Correspondence and requests for materials should be addressed to P.J.D. (pauldurack@llnl.gov).

References and Notes

1. M. R. Allen, W. J. Ingram, Constraints on future changes in climate and the hydrologic cycle. *Nature* **419**, 224 (2002).
2. I. M. Held, B. J. Soden, Robust Responses of the Hydrological Cycle to Global Warming. *Journal of Climate* **19**, 5686 (2006).
3. F. J. Wentz, L. Ricciardulli, K. Hilburn, C. Mears, How Much More Rain Will Global Warming Bring? *Science* **317**, 233 (July 13, 2007, 2007).
4. G. L. Stephens, T. D. Ellis, Controls of Global-Mean Precipitation Increases in Global Warming GCM Experiments. *Journal of Climate* **21**, 6141 (2008).
5. S. Emori, S. J. Brown, Dynamic and thermodynamic changes in mean and extreme precipitation under changed climate. *Geophys Res Lett* **32**, L17706 (2005).
6. G. A. Meehl *et al.*, The WCRP CMIP3 multimodel dataset - A new era in climate change research. *B Am Meteorol Soc* **88**, 1383 (Sep, 2007).
7. C. Chou, J. D. Neelin, C.-A. Chen, J.-Y. Tu, Evaluating the “Rich-Get-Richer” Mechanism in Tropical Precipitation Change under Global Warming. *Journal of Climate* **22**, 1982 (2009/04/01, 2009).
8. G. L. Stephens *et al.*, Dreary state of precipitation in global models. *Journal of Geophysical Research* **115**, D24211 (2010).
9. V. Ramanathan, P. J. Crutzen, J. T. Kiehl, D. Rosenfeld, Aerosols, Climate, and the Hydrological Cycle. *Science* **294**, 2119 (December 7, 2001, 2001).
10. Y. Ming, V. Ramaswamy, G. Persad, Two opposing effects of absorbing aerosols on global-mean precipitation. *Geophys Res Lett* **37**, L13701 (2010).
11. K. E. Trenberth *et al.*, in *Climate Change 2007: The Physical Science Basis. Contribution of the Working Group I to the Fourth Assessment Report of the Intergovernmental Panel on Climate Change,* S. Solomon *et al.*, Eds. (Cambridge University Press, Cambridge UK and New York USA, 2007), pp. 235-336.
12. X. Zhang *et al.*, Detection of human influence on twentieth-century precipitation trends. *Nature* **448**, 461 (2007).
13. J. J. Schanze, R. W. Schmitt, L. L. Yu, The global oceanic freshwater cycle: A state-of-the-art quantification. *Journal of Marine Research* **68**, 569 (2010).
14. Y. Tian *et al.*, Component analysis of errors in satellite-based precipitation estimates. *Journal of Geophysical Research* **114**, D24101 (2009).
15. X. Yin, A. Gruber, P. Arkin, Comparison of the GPCP and CMAP Merged Gauge–Satellite Monthly Precipitation Products for the Period 1979–2001. *Journal of Hydrometeorology* **5**, 1207 (2004).
16. A. Dai, I. Y. Fung, A. D. Del Genio, Surface Observed Global Land Precipitation Variations during 1900–88. *Journal of Climate* **10**, 2943 (1997).
17. P. A. Arkin, T. M. Smith, M. R. P. Sapiano, J. Janowiak, The observed sensitivity of the global hydrological cycle to changes in surface temperature. *Environmental Research Letters* **5**, 035201 (2010).
18. K. M. Lau, H. T. Wu, Detecting trends in tropical rainfall characteristics, 1979–2003. *International Journal of Climatology* **27**, 979 (2007).
19. J. Liu, T. Xiao, L. Chen, Intercomparisons of Air–Sea Heat Fluxes over the Southern Ocean. *Journal of Climate* **24**, 1198 (2011).
20. A. Dai, T. Qian, K. E. Trenberth, J. D. Milliman, Changes in Continental Freshwater Discharge from 1948 to 2004. *Journal of Climate* **22**, 2773 (2009).
21. G. Wüst, in *Länderkundliche research, Festschrift* (Norbert Krebs, Hermann-Wagner-Gedachtnisschrift, 1936), pp. 347-359.
22. P. J. Durack, S. E. Wijffels, N. L. Bindoff, Ocean Salinity: A Water Cycle Diagnostic? . *B Am Meteorol Soc* **92**, s91 (2011).
23. R. W. Schmitt, Salinity and the Global Water Cycle. *Oceanography* **21**, 14 (Mar, 2008).
24. T. P. Boyer, S. Levitus, J. I. Antonov, R. A. Locarnini, H. E. Garcia, Linear trends in salinity for the World Ocean, 1955-1998. *Geophys Res Lett* **32**, L01604 (2005).

25. P. J. Durack, S. E. Wijffels, Fifty-Year Trends in Global Ocean Salinities and Their Relationship to Broad-Scale Warming. *Journal of Climate* **23**, 4342 (2010).
26. K. P. Helm, N. L. Bindoff, J. A. Church, Changes in the global hydrological-cycle inferred from ocean salinity. *Geophys Res Lett* **37**, L18701 (2010).
27. S. Hosoda, T. Sugo, N. Shikama, K. Mizuno, Global Surface Layer Salinity Change Detected by Argo and Its Implication for Hydrological Cycle Intensification. *Journal of Oceanography* **65**, 579 (2009).
28. H. Freeland *et al.*, in *Proceedings of OceanObs'09: Sustained Ocean Observations and Information for Society,* J. Hall, D. E. Harrison, D. Stammer, Eds. (Venice, Italy, 2010), vol. 2.
29. J.-L. Lin, The Double-ITCZ Problem in IPCC AR4 Coupled GCMs: Ocean–Atmosphere Feedback Analysis. *Journal of Climate* **20**, 4497 (2007).
30. G. A. Meehl *et al.*, in *Climate Change 2007: The Physical Science Basis. Contribution of the Working Group I to the Fourth Assessment Report of the Intergovernmental Panel on Climate Change,* S. Solomon *et al.*, Eds. (Cambridge University Press, Cambridge UK and New York USA, 2007), pp. 747-845.

Figures

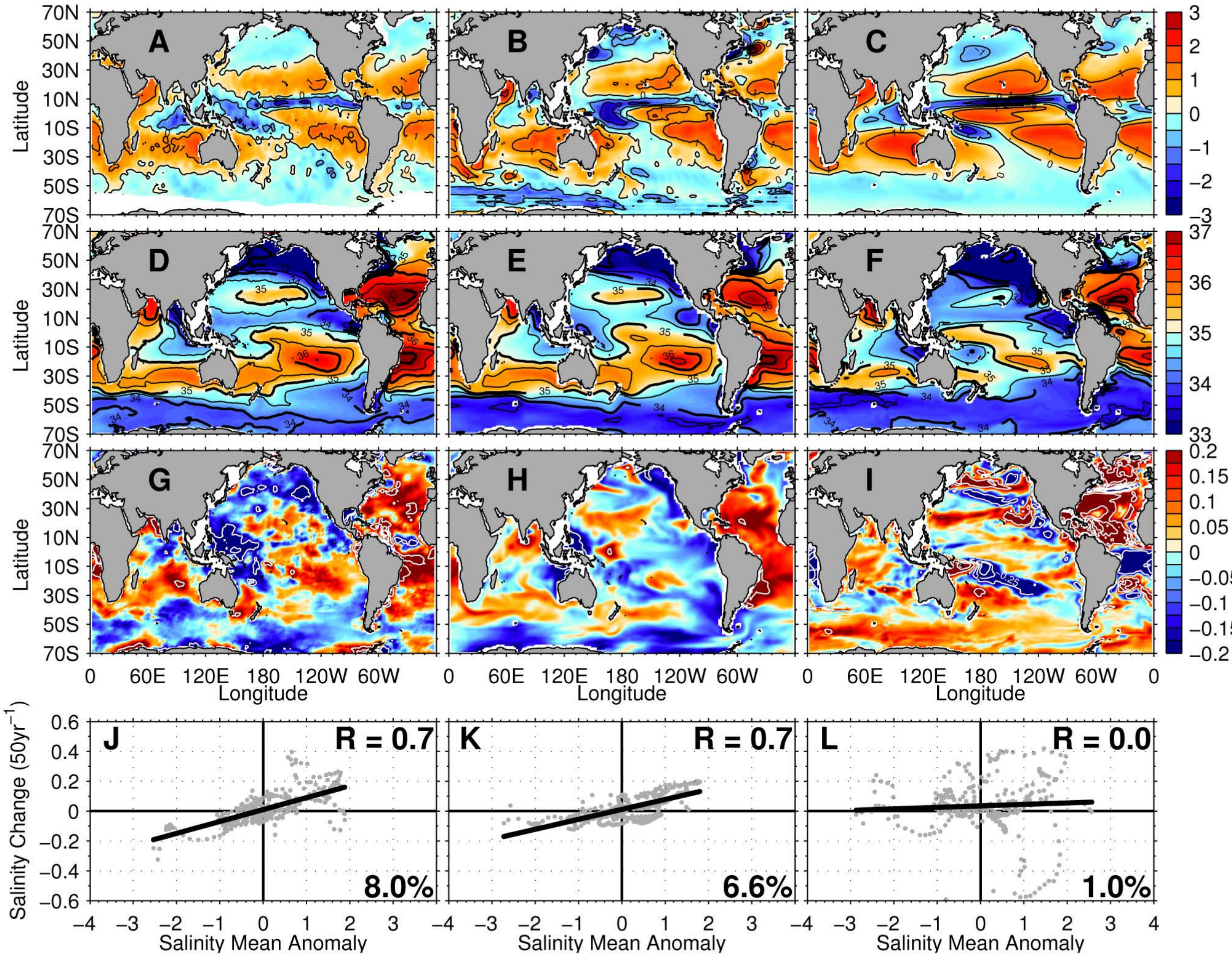

Figure 1. Observed and selected CMIP3 20C3M simulations of surface salinity and water fluxes. Surface mean water flux 1950-2000 (E-P m yr^{-1}; A, B, C). Surface mean salinity 1950-2000 (PSS-78; D, E, F). Surface salinity change 1950-2000 (PSS-78 50 yr^{-1}; G, H, I). Basin zonal-mean surface salinity trends (y-axis) versus surface mean salinity anomaly (with surface basin zonal mean removed; PA & PC; J, K, L). The observed result of Durack & Wijffels (2010; D, G, J) and (A) the observed result of Josey *et al*. (1998) for 1980-1993. Results from the Canadian Centre for Climate Modelling & Analysis: CGCM3.1 (T63) model (B, E, H, K), and results from the United Kingdom MetOffice: HadGEM1 model (C, F, I, L). For A-C black contours every 1 m yr^{-1}. For D-F, black contours represent surface mean salinity every 1 PSS-78 for bold lines and 0.5 for thin. For G-I, white contours represent surface salinity change every 0.25 PSS-78.

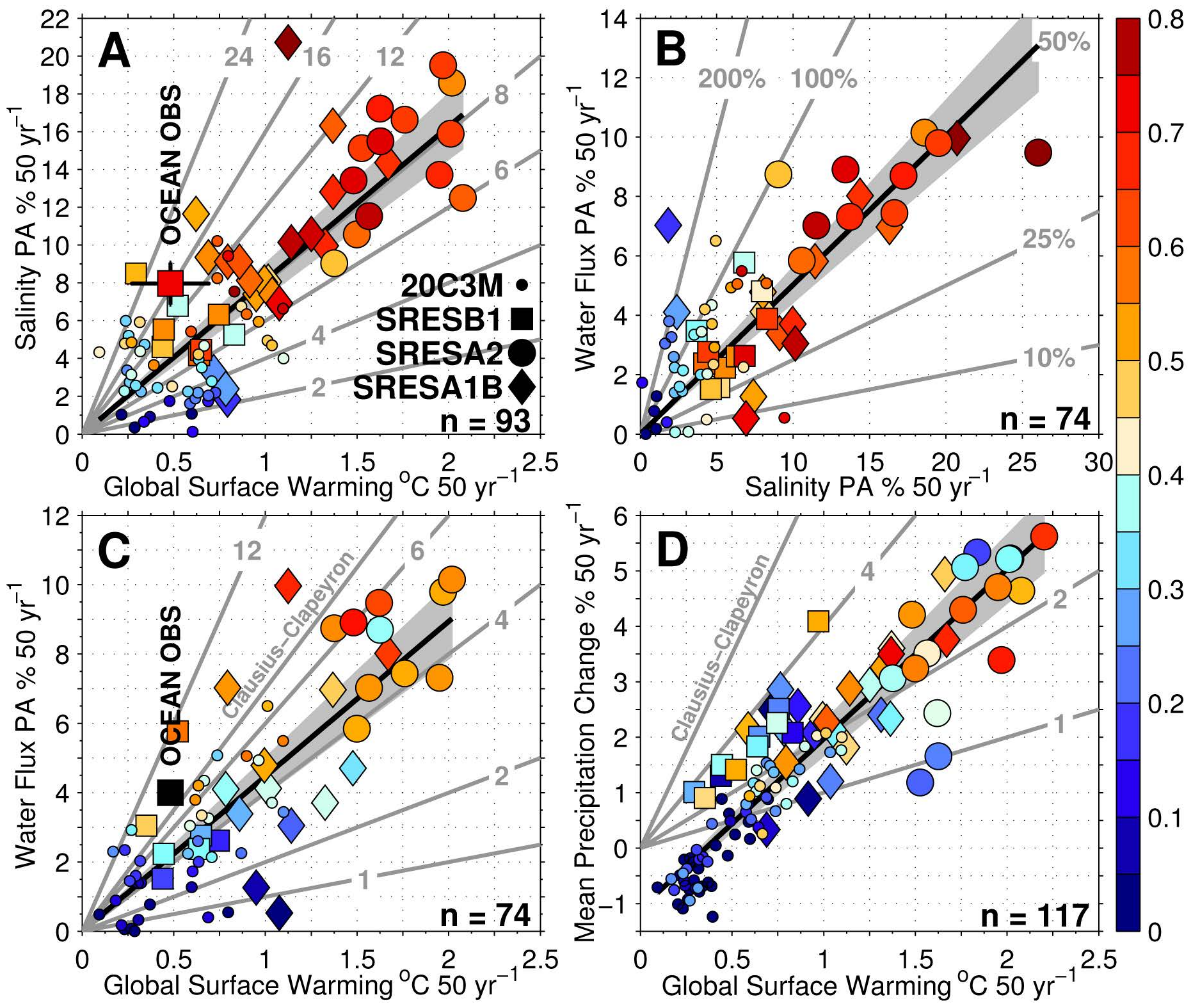

Figure 2. Pattern amplification and pattern correlations from the available CMIP3 simulations compared to new observational estimates. The number of individual simulations which have been analysed for each variable is noted in the bottom right hand corner of each panel. A) The surface salinity pattern amplification (PA; y-axis) versus the corresponding global average surface temperature change (ΔTa; x-axis), colours are the salinity pattern correlation (PC). B) Water flux (E-P; y-axis) PA versus surface salinity PA (x-axis), colours are the salinity pattern correlation (PC). C) Water flux (E-P; y-axis) PA versus global average surface temperature change (ΔTa; x-axis), colours are the E-P pattern correlation (PC). D) Global spatial average precipitation change, rather than pattern amplification (ΔP; y-axis) versus global average surface temperature change (ΔTa; x-axis), colours are the precipitation PC. Grey lines express constant proportional change. Grey shading (99% C.I.) bounds the PC-weighted linear best fit to the model ensemble for a line intersecting 0 (y-axis; A, B, C) and -1.1 (y-axis; D) in black. The 20th century (20C3M; 1950-2000) simulations are presented in small circles, and the three 21st century projected scenarios (SRES; 2050-2099) are shown as squares for B1, large circles for A2 and diamonds for A1B. All simulations have been de-drifted using an appropriate pre-industrial control simulation for the period 1900-2049.

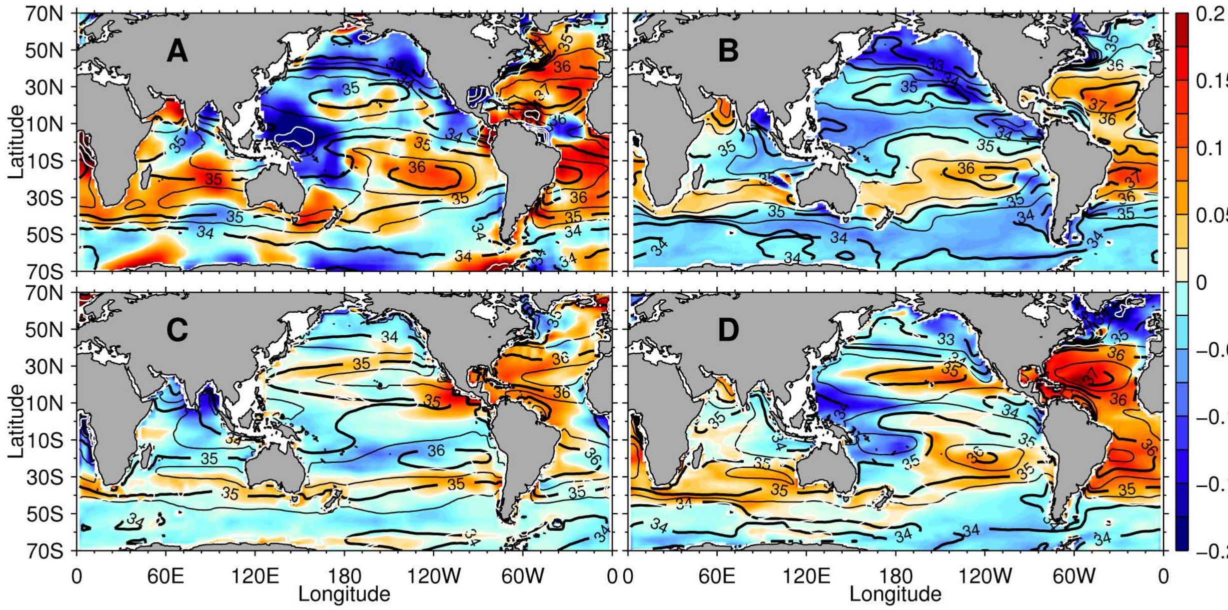

Figure 3. Patterns of 50-year surface salinity change (PSS-78 $50yr^{-1}$). A) The 1950-2000 observational result of Durack & Wijffels (2010). B) From an ocean model forced with an idealised surface 5% E-P enhancement ($50\ yr^{-1}$; see text). C) For an ensemble mean from 1950-2000 of the CMIP3 20C3M simulations which warm less than <0.5°C (24 simulations; see Table S2). D) For an ensemble mean from 1950-2000 of the CMIP3 20C3M simulations which warm greater than >0.5°C (26 simulations; see Table S2). In each panel, the corresponding mean salinity from each representative data source is contoured in black, with thick lines every 1 (PSS-78) and thin lines every 0.5 (PSS-78).

Supporting Online Material for

Ocean Salinities Reveal Strong Global Water Cycle Intensification during 1950-2000

Paul J. Durack*, Susan E. Wijffels and Richard J. Matear

*To whom correspondence should be addressed. E-mail: pauldurack@llnl.gov

Published XX Month Year on Science Express
DOI: 10.1126/science.XXXXXXX

This PDF file includes:
SOM Text
Figs. S1 to S9
Tables S1 to S3
References

Supporting Online Material

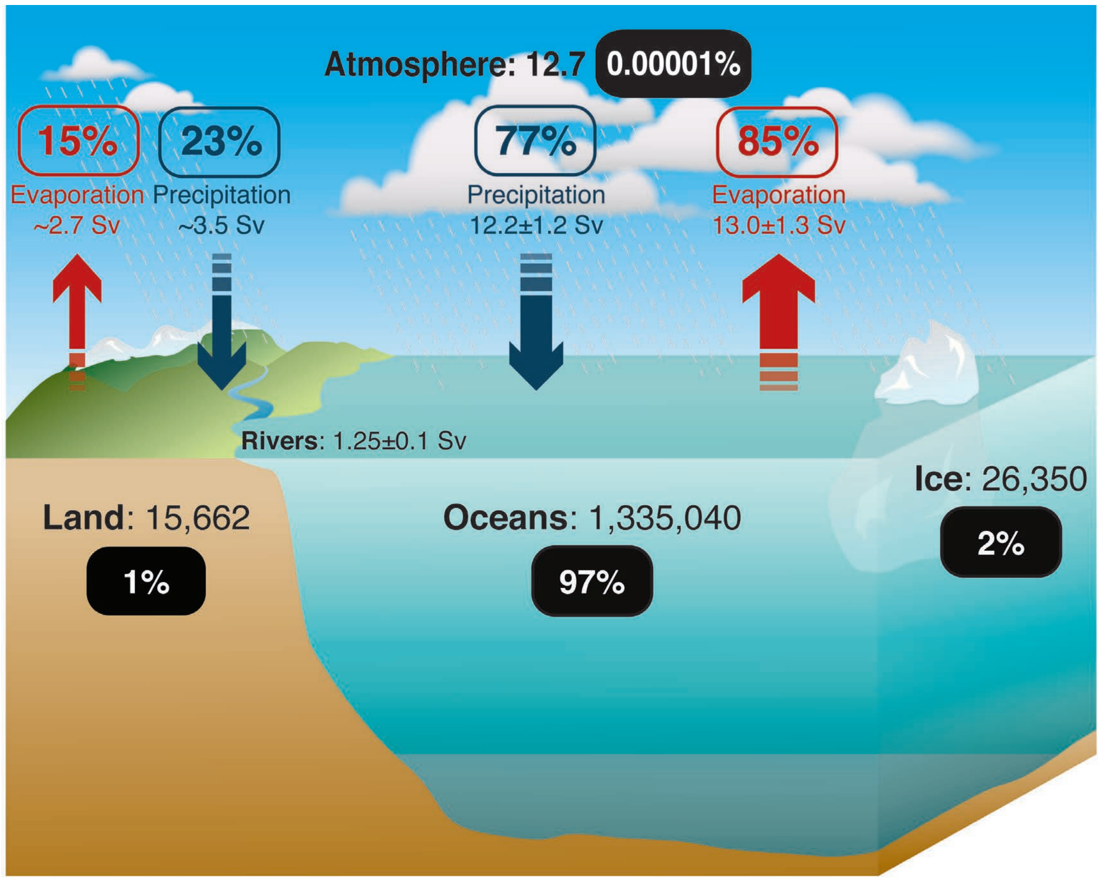

Reservoirs represented by solid boxes: 10^3 km^3, fluxes represented by arrows: Sverdrups (10^6 m^3 s^{-1})
Sources: Baumgartner & Reichel, 1975; Schmitt, 1995; Trenberth et al., 2007; Schanze et al., 2010

Figure S1. Adapted schematic (after Schmitt, 1995 and updated after Trenberth *et* al., 2007 and Schanze *et al.*, 2010) represents the key role of the ocean in the global water cycle – around 80% of the Earth's surface water fluxes occur at the ocean surface. Reservoir estimates represent storages in 10^3 km^3, flux estimates represent transports in Sverdrups (10^6 m^3 s^{-1}) and values within boxes represent the approximate percentage of total storages (black boxes) or flux estimates (rainfall = blue; evaporation = red) for the global surface.

Observational surface salinity change analysis

For this analysis, new estimates of the surface salinity climatological mean and the 50-year (1950-2000) surface salinity change fields were obtained. These analyses used both the available quality-controlled historical hydrographic profiles, along with more recent data from the global Argo Program to determine long-term trends over the 50-year timescale (Durack & Wijffels, 2010).

The results presented in this analysis provide a broad-scale, globally consistent view of coherent, long-term global salinity changes which agree with many of the long-term regional salinity changes presented in many independent studies (Durack & Wijffels, 2010 - Table 1; Durack *et al*., 2011). The key advantages of the new approach are its near global coverage (marginal seas and high-latitude seas >70° are excluded), and the methodology which is optimised to reduce biases due to seasonal and spatial sampling, particularly in the historical data, by fitting the mean climatology and trends concurrently. An attempt to remove biases associated with strong ENSO cycles is also an advantage of this analysis. In the sparsely historically observed Southern Hemisphere oceans, the analysis relies on Argo's ability to highly resolve the mean, seasonal and ENSO ocean responses. This methodology reduces aliasing by these observed phenomena into the multidecadal trend, with a 50-year temporal analysis long enough to account for many modes of cyclical climate variability. Due to the availability of ocean profile data, the varied temporal global sampling also means that any "simple" average represents different eras in different parts of the ocean (Durack & Wijffels, 2010; Figure 2B, D), and by fitting the trend and mean climatology at the same time, errors due to a biased climatology are avoided.

Comparisons to previous observational surface salinity change estimates

Many estimates of salinity changes throughout the global ocean have been published. We selected two key global studies (Boyer *et al*., 2005; Hosoda *et al*., 2009) and provide quantified comparisons to directly compare the robustness of salinity pattern amplification magnitudes between independent estimates. As noted in some detail in Durack & Wijffels (2010, Table 1) many salinity change estimates exist, and the results presented by Durack & Wijffels (2010) tend to agree with the broad-scale conclusions of previous estimates of change.

In order to quantitatively compare the surface salinity results it was necessary to form global zonal means for both climatological mean surface salinity and the surface trend fields for the representative studies. This analysis differs from the main text, as basin zonal, rather than global zonal means have been used. In the case of Boyer *et al*. (2005) their data is freely downloadable off the NODC website. For Hosoda *et al*. (2009) only their global zonal mean values were available from their published figures 2A and 2B. For comparison, Figure S2 captures the global zonal mean results for each study.

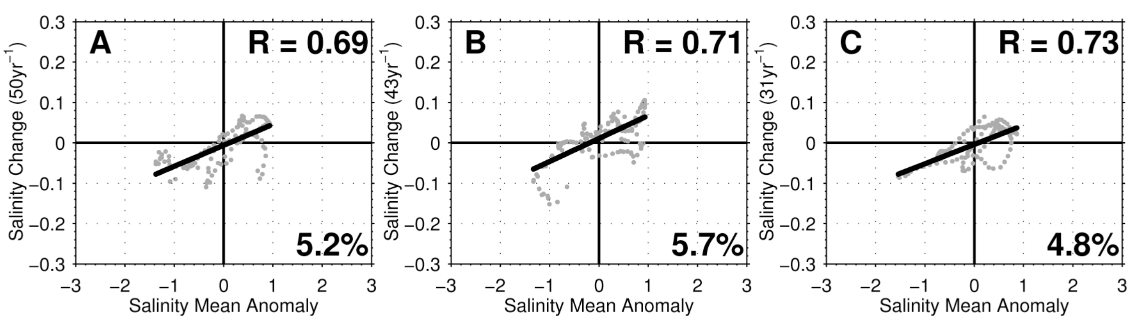

Figure S2. Global zonal mean surface salinity comparison for the analyses of A) Durack & Wijffels (2010), B) Boyer *et al*. (2005) and C) Hosoda *et al*. (2009; using their global zonal mean results)

It is clear that each independent study suggests that the "rich get richer" mechanism is operating upon ocean salinity, with a linear relationship present in each analysis suggesting fresh waters are getting fresher and salty waters are getting saltier. They all share similar spatial pattern correlation (PC) values of ~0.7, however magnitudes of PA are more variable, with the Durack & Wijffels (2010) estimate (A) suggesting a representative median value for these three independent studies of ~5% over their 50-years of analysis.

CMIP3: Model drift correction

Model (or climate) drift is an inherent problem in current state-of-the-art climate modelling systems. Drift is the term applied to a systematic bias in model fields, which can be attributed to deficiencies in the modelling system, with this feature primarily a problem with ocean simulations. These manifest due to many different reasons, primarily on two timescales. Rapid drift occurs and is most likely due to errors introduced when coupling the ocean and atmosphere model subcomponents, and is referred to as "coupling shock". Longer term drift can be attributed to the slow adjustment of the modelled deep ocean, and the most likely causes of this drift can be linked to unresolved/sub-grid scale physics (exclusion of eddies, localised boundary flows), poor initialisation (deficiencies with "first/best guess" climatologies), imposed flux adjustments (mostly deprecated in CMIP3) and insufficient model "spin-up" (incomplete initialisation of the coupled model, so that a pseudo-equilibrium climate state in the model is never reached).

In order to effectively obtain the most accurate estimate of the transient greenhouse gas (GHG) forced signal from a climate model simulation, and in particular the low signal-to-noise externally forced 20C3M simulations, it is necessary to attempt to account for drift. It is also necessary to attempt to account for high and low-frequency variability, which can influence resolved trends. For this reason multidecadal trends over 50-years (1950-2000) are considered in this analysis, with an expectation that modelled climate variability will be fairly small over 50-year timescales when compared to the transient GHG-forced response (see following CMIP3: Assessment of Modelled Internal Variability section and Figure S4). For the analysis presented here, drift was determined from the 1900-2049 period associated with the initial (run1: 1950-2000) 20C3M simulation, and the spatial pattern and magnitude was then removed from all the transient 20C3M simulations for each representative simulation. A test was undertaken to ensure that the differences in the time of 20C3M initialisation of the corresponding PICNTRL did not largely affect the result, and this was found to be a sound assumption, with the exception of the gfdl_cm2_0 run1. However as salinity was only available for run1 (and not the subsequent run2 or run3) for this model it didn't affect the analysis. The 1900-2049 period was selected as it bounded 1950-2000 (50-years either side), the period over which trends were obtained from 20C3M simulations and directly compared to the new observed estimates for the same period. Additionally, use of this early period ensured a larger ensemble of CMIP3 data was available, as available PICNTRL runs tend not to extend beyond 2100.

In order to test the sensitivity to this method of drift removal, a duplicated analysis was undertaken using the 2000-2149 period - this period bounding 2050-2099, the period over which SRES analyses were undertaken. A decrease in the total number of simulations available for this analysis was found, due to a reduction in available concurrent PICNTRL data (Figure S3 vs Figure 2), however they key results expressed in Figure 2 are largely reproduced in this adapted analysis (Figure S3).

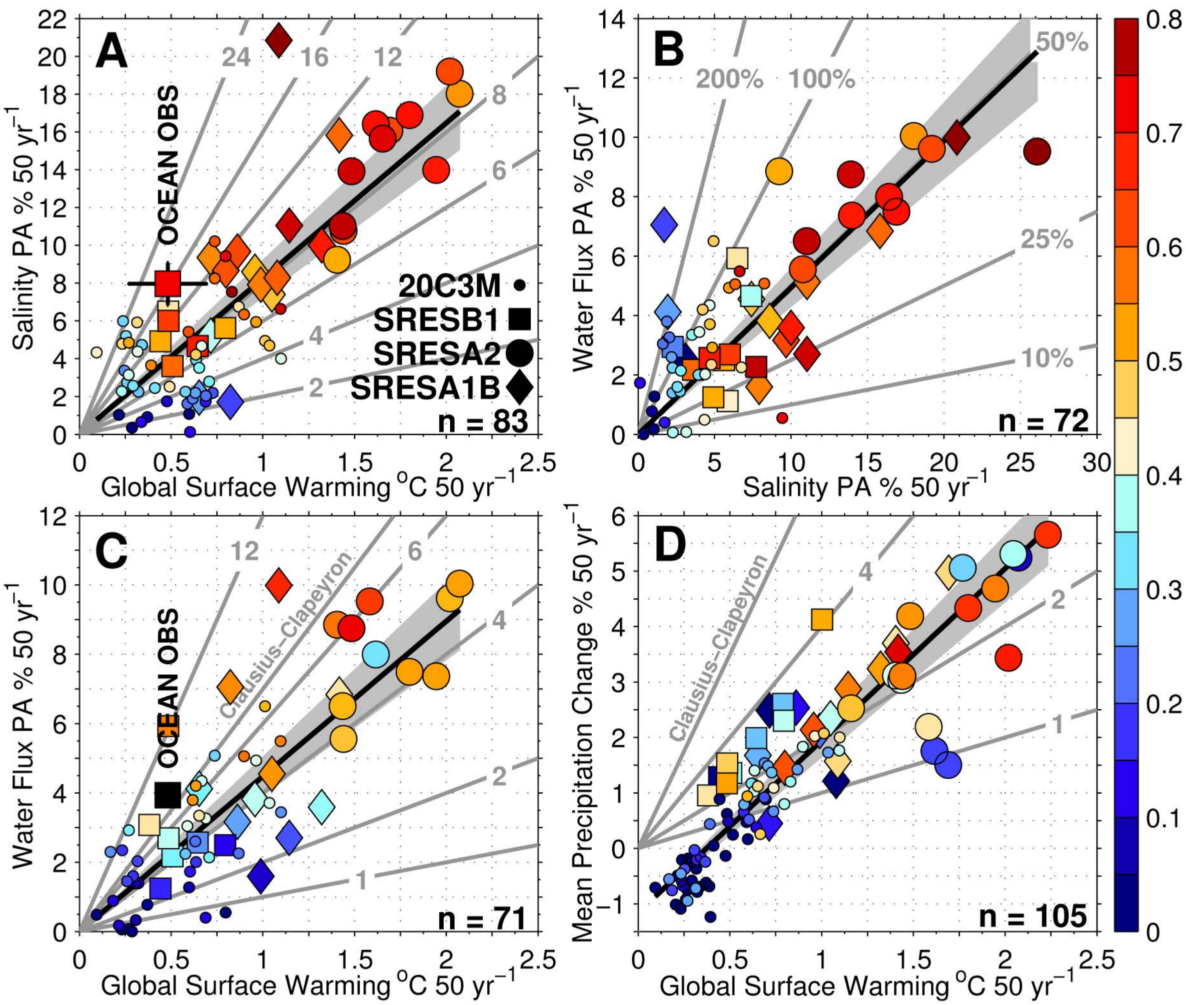

Figure S3. Representative change responses from the available CMIP3 simulations compared to new observational estimates of ocean salinity changes. Following Figure 2, however all SRES fields have been de-drifted using an appropriate pre-industrial control simulation for the period 2000-2149, rather than 1900-2049 (Fig. 2). The number of individual simulations which have been analysed for each variable is noted in the bottom right hand corner of each panel. A) The surface salinity pattern amplification (PA; y-axis) versus the corresponding global average surface temperature change (ΔTa; x-axis), colours are the salinity pattern correlation (PC). B) Water flux (E-P; y-axis) PA versus surface salinity PA (x-axis), colours are the salinity pattern correlation (PC). C) Water flux (E-P; y-axis) PA versus global average surface temperature change (ΔTa; x-axis), colours are the E-P pattern correlation (PC). D) Global spatial average precipitation change, rather than pattern amplification (ΔP; y-axis) versus global average surface temperature change (ΔTa; x-axis), colours are the precipitation PC. Grey lines express constant proportional change. Grey shading (99% C.I.) bounds the correlation-weighted linear best fit to the model ensemble for a line intersecting 0 (y-axis; A, B, C) and -1.2 (y-axis; D) in black. The 20th century (20C3M; 1950-2000) simulations are presented in small circles, and the three 21st century projected scenarios (SRES; 2050-2099) are shown as squares for B1, large circles for A2 and diamonds for A1B.

CMIP3: Assessment of Modelled Internal Variability

To further test whether modelled variability has influenced the CMIP3 results an additional analysis was undertaken to compare the 50-year (1950-2000; 20C3M) analysed results to change patterns obtained over the full length (~150-years) of the simulations expressed in Figure 1. As observational data coverage is only available for 1950-onwards, this test is not possible for the observational estimates. However, investigating modelled variability is insightful when considering what is cyclical versus transient change. For this additional analysis, surface salinity patterns were assessed for their full temporal trends, so 1850-2000 for the cccma_cgcm3_1_t63 and 1860-2000 for ukmo_hadgem1.

The observed result presented in Figure 1J is reproduced below (Figure S4A). To further enhance variability the full spatial analysis is considered, rather than the zonal ocean basin averages presented in Figures 1 & 2. When comparing the results from this full grid analysis (Figure S4A) to the zonal mean analysis (Figure 1J) it is clear that spatial smoothing has enhanced the pattern correlation (PC; 0.5 – Figure S4A vs 0.7 Figure 1J). However, the surface salinity pattern amplification (PA) is approximately equivalent for each of the analyses; 7.7% (Figure S4A) compared to 8% (Figure 1J). Model analyses for 50-years are presented in Figure S4B, C and ~150-years in Figure S4D, E respectively. Considering the cccma_cgcm3_1_t63 model and the 50-year analysis, a slight increase in PC is also apparent due to the spatial smoothing (0.7 Figure 1K vs 0.6 Figure S4B), however reported PA is 6.1% for both the 50-year (Figure S4B) and ~150-year analysis (Figure S4D), with a decrease in PC for the ~150-years (0.6 vs 0.5). For ukmo_hadgem1 similar results are found, with similar PA values recorded across all analyses (1.0% Figure 1L vs 0.6% and 0.4% Figure S4C, E) and correspondingly low PC. This additional analysis supports the use of the 50-year periods used in this study, as these 50-year periods are truly representative of the full 20th century simulated change (Figure S4).

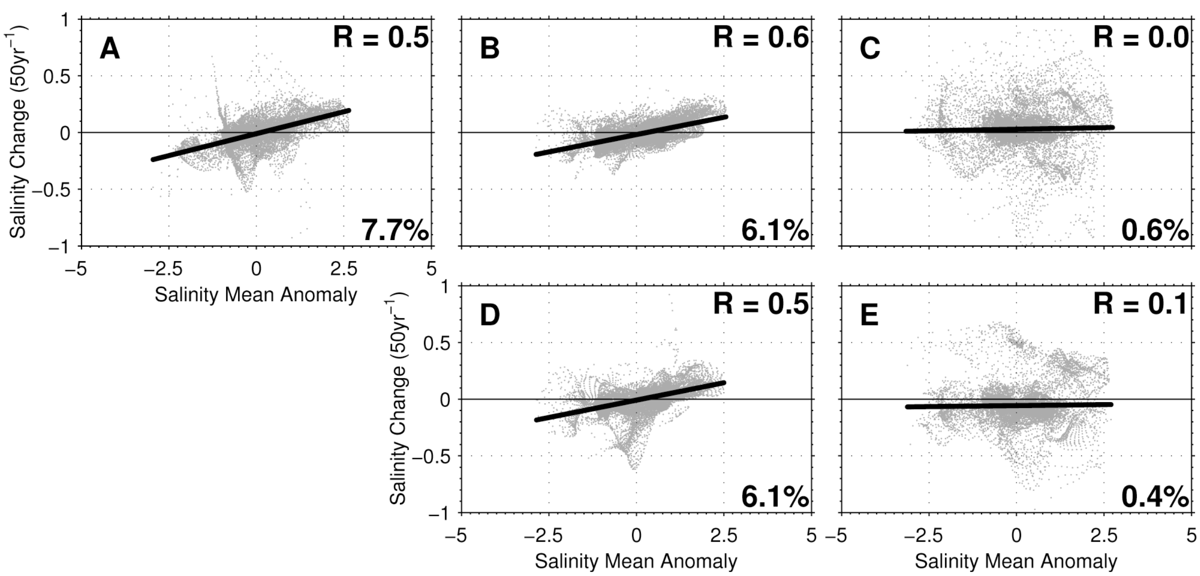

Figure S4. Examples of pattern amplification for global ocean surface salinity – values are plotted point-wise for the analysed surface response. Unlike Figure 1, fields are not spatially smoothed using the basin zonal mean approach. for A) the 1950-2000 observed result B) Canadian Centre for Climate Modelling & Analysis: CGCM3.1 (T63) for 1950-2000 C) United Kingdom MetOffice: HadGEM1 for 1950-2000 D) Canadian Centre for Climate Modelling & Analysis: CGCM3.1 (T63) for 1850-2000 E) United Kingdom MetOffice: HadGEM1 for 1860-2000

CMIP3: The Role of Aerosols and other Forcing Agents

The effect of comprehensive aerosol schemes is known to provide a general cooling effect and a corresponding dampening effect on local water cycle operation (Ramanathan *et al*., 2001; Ming *et* al., 2010; Chen *et al*., 2011). In CMIP3 20C3M simulations which incorporate volcanic aerosols forcing also generally include other aerosol effects such as black and organic carbon and sulphates (Table S1).

Table S1. Forcings and flux corrections used in CMIP3 simulations of 20th century climate change (Updated from Santer *et al*., 2007). The letter 'Y' denotes inclusion of the specific forcing for the selected model. G: well-mixed greenhouse gases; O: tropospheric and stratospheric ozone; SD: sulphate aerosol direct effects; SI: sulphate aerosol indirect effects; BC: black carbon; OC: organic carbon; MD: mineral dust; SS: sea salt; LU: land use change; SO: solar irradiance; VL: volcanic aerosols. For flux corrections (FC) the following notation is used; Freshwater: F; Heat/momentum: H.

Model	Representative numbers	G	O	SD	SI	BC	OC	MD	SS	LU	SO	VL	FC
bccr_bcm2.0	1	Y	-	Y	-	-	-	-	-	-	-	-	-
cccma_cgcm3_1_t47	2,3,4,5,6	Y	-	Y	-	-	-	-	-	-	-	-	F,H
cccma_cgcm3_1_t63	7	Y	-	Y	-	-	-	-	-	-	-	-	F,H
cnrm_cm3	8	Y	Y	Y	-	Y	-	-	-	-	-	-	-
csiro_mk3_0	9,10,11	Y	Y	Y	-	-	-	-	-	-	-	-	-
csiro_mk3_5	12,13,14	Y	Y	Y	-	-	-	-	-	-	-	-	-
gfdl_cm2_0	15	Y	Y	Y	-	Y	Y	-	-	Y	Y	Y	-
gfdl_cm2_1	16	Y	Y	Y	-	Y	Y	-	-	Y	Y	Y	-
giss_aom	17,18	Y	-	Y	-	-	-	-	Y	-	-	-	-
giss_model_e_h	19,20,21,22,23	Y	Y	Y	Y	Y	Y	Y	Y	Y	Y	Y	-
giss_model_e_r	24,25,26,27,28,29,30,31,32	Y	Y	Y	Y	Y	Y	Y	Y	Y	Y	Y	-
iap_fgoals1_0	33,34,35	Y	-	Y	-	-	-	-	-	-	-	-	-
ingv_echam4	36	Y	Y	Y	-	-	-	-	-	-	-	-	-
ipsl_cm4	37	Y	-	Y	Y	-	-	-	-	-	-	-	-
miroc3_2_hires	38	Y	Y	Y	Y	Y	Y	Y	Y	Y	Y	Y	-
miroc_3_2_medres	39	Y	Y	Y	Y	Y	Y	Y	Y	Y	Y	Y	-
miub_echo_g	40,41,42	Y	-	Y	Y	-	-	-	-	-	Y	Y	F,H
mpi_echam5	43,44,45	Y	Y	Y	Y	-	-	-	-	-	-	-	
mri_cgcm2_3_2a	46,47,48,49,50	Y	-	Y	-	-	-	-	-	-	Y	Y	F,H
ncar_ccsm3_0	51,52	Y	Y	Y	-	Y	Y	-	-	-	Y	Y	
ncar_pcm1	53,54,55	Y	Y	Y	-	-	-	-	-	-	Y	Y	
ukmo_hadcm3	56,57	Y	Y	Y	Y	-	-	-	-	-	Y	-	
ukmo_hadgem1	58	Y	Y	Y	Y	Y	Y	-	-	Y	Y	-	

So how do aerosols affect the reported water cycle changes as expressed in surface salinity, surface water flux pattern amplification (PA) and corresponding pattern correlations (PC)? The results presented in Figure 2 included all available simulation results from the 20C3M as well as the available SRES (A1B, A2 and B1) simulations. As volcanic aerosol emissions are not readily predictable into the future, these agents were excluded from SRES simulations, however have been included in around half of the available 20C3M simulations (Table S1).

Representative change responses for many aspects of water cycle operation were presented in Figure 2. To concentrate on aerosol effects, Figure S5 reproduces the results presented in Figure 2A, B just for the 20C3M simulations. This sub-suite of simulations can then be assessed on whether they included volcanic aerosol effects, or whether they didn't (Table S1).

There appears to be a clear pattern of enhanced global surface warming in non-volcanic models (Figure S5A; contrast circles vs diamonds), with corresponding larger PA (Figure S5A colours) when compared to the volcanically-forced simulations. A clear pattern of low-warming simulations with low PA (Figure S5A; left-bottom), compared to high-warming simulations with comparatively higher PA (Figure S5A; right-top) is apparent. This tends to suggest that a clear signal-to-noise process is in operation, with a more coherent salinity PA response expressed in the stronger warming simulations, whereas many of the low-warming simulations show no such coherent salinity PA. When comparing the PA of both surface salinity and surface water flux (Figure S5B) this clear split appears even more clearly, with low salinity PA simulations also having low water flux PA (Figure S5B; left-bottom) and simulations with comparatively high salinity PA also having high surface water flux PA. There appears a clear increase in PA (Figure S5B; colours – blue to red) from the lower left (noise) to the upper right (signal), with simulations with large PA values tending to be those which report a larger warming (Figure S5A).

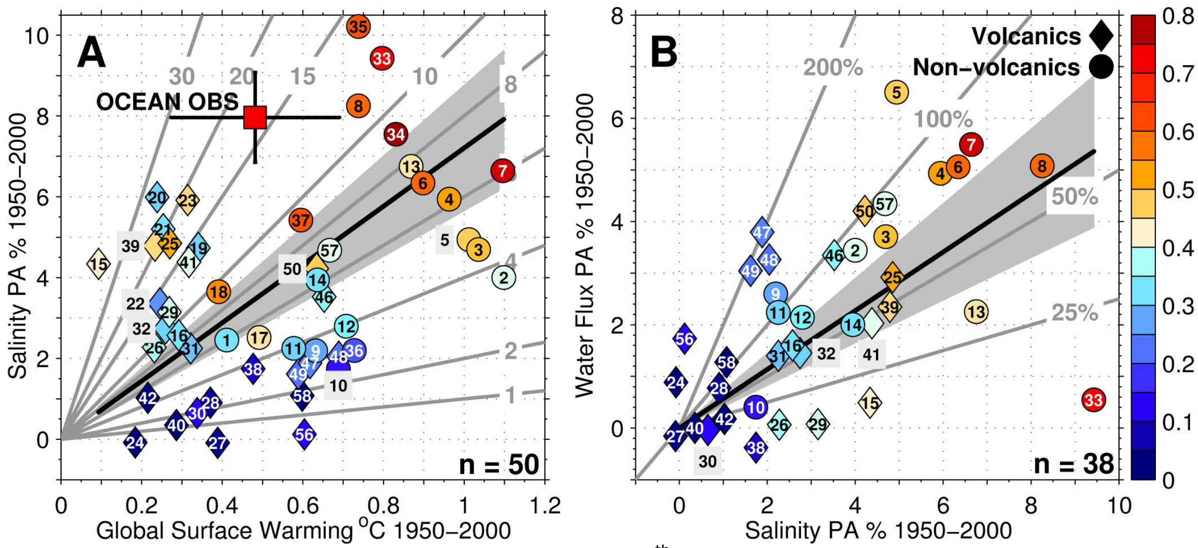

Figure S5. Pattern amplification (PA) rates for all available 20th century (20C3M; 1950-2000) de-drifted CMIP3 simulations. Diamonds represent 20C3M simulations which include volcanic aerosol forcing, circles are simulations without volcanic aerosol forcing. The number of individual simulations which have been analysed for each variable is noted in the bottom right hand corner of each panel. For A) Surface salinity (y-axis) versus the corresponding global average surface temperature change (ΔTa; x-axis). B) Water flux (E-P; y-axis) versus surface salinity (x-axis). Colours are the salinity pattern correlation (PC) for both panels A & B. Grey lines express constant proportional change. Grey shading (99% C.I.) bounds the correlation-weighted linear best fit to the model ensemble for a line intersecting 0 in black.

The full ranges of CMIP3 20C3M change responses for 1950-2000 are contained in Table S2. These results include global change estimates for the 5 variables analysed, including; salinity and water flux (E-P) pattern amplification, ocean and global surface temperature and global mean rainfall changes (ΔP). For reference a comparative non-exhaustive selection of observed estimates from available data products is also included in the lower section of Table S2. The range of surface salinity responses, and spatial patterns of the associated drift estimates (see section above), along with 1950-2000 climatological surface salinity and water flux (E-P) means are contained in Figure S6.

Table S2. Integrated global surface values for 1950-2000 trends resolved from available 20th century (20C3M) CMIP3 experiments, de-drifted by their corresponding pre-industrial control in: sea surface salinity (basin zonal-mean) pattern amplification (PA; %), ocean water flux (E-P) (basin zonal-mean) pattern amplification (PA; %), area-weighted global ocean surface temperature (°C), area-weighted global surface temperature (°C) and area-weighted global surface mean precipitation change (%). A non-exhaustive selection of observational estimates from available data products are found in the lower section of the table for comparison. Trends have been obtained over the period in parentheses and scaled to represent directly comparable 50-yr changes.

#	Model	Salinity (%PA)	E-P (%PA)	Ocean Temperature (°C)	Global Temperature (°C)	Rainfall (ΔP)
1	bccr_bcm2_0.20c3m.run1	+2.5	-	-	+0.41	+0.1
2	cccma_cgcm3_1_t47.20c3m.run1	+4.0	+3.4	+0.73	+1.10	+2.0
3	cccma_cgcm3_1_t47.20c3m.run2	+4.7	+3.7	+0.66	+1.04	+1.7
4	cccma_cgcm3_1_t47.20c3m.run3	+5.9	+4.9	+0.66	+0.96	+2.0
5	cccma_cgcm3_1_t47.20c3m.run4	+4.9	+6.5	+0.67	+1.01	+2.1
6	cccma_cgcm3_1_t47.20c3m.run5	+6.3	+5.1	+0.61	+0.90	+1.8
7	cccma_cgcm3_1_t63.20c3m.run1	+6.6	+5.5	+0.74	+1.10	+1.8
8	cnrm_cm3.20c3m.run1	+8.3	+5.1	-	+0.74	+1.1
9	csiro_mk3_0.20c3m.run1	+2.2	+2.6	+0.42	+0.63	+1.0
10	csiro_mk3_0.20c3m.run2	+1.7	+0.4	+0.45	+0.69	+0.9
11	csiro_mk3_0.20c3m.run3	+2.2	+2.2	+0.38	+0.58	+0.8
12	csiro_mk3_5.20c3m.run1	+2.8	+2.1	+0.44	+0.71	+1.5
13	csiro_mk3_5.20c3m.run2	+6.8	+2.3	+0.59	+0.87	+1.4
14	csiro_mk3_5.20c3m.run3	+3.9	+2.0	+0.47	+0.64	+1.1
15	gfdl_cm2_0.20c3m.run1	+4.3	+0.5	+0.02	+0.09	-0.7
16	gfdl_cm2_1.20c3m.run2	+2.6	+1.6	+0.21	+0.29	-0.6
17	giss_aom.20c3m.run1	+2.5	-	+0.35	+0.49	+0.5
18	giss_aom.20c3m.run2	+3.7	-	+0.27	+0.39	+0.4
19	giss_model_e_h.20c3m.run1	+4.7	-	-	+0.34	-0.2
20	giss_model_e_h.20c3m.run2	+6.0	-	-	+0.24	-0.6
21	giss_model_e_h.20c3m.run3	+5.2	-	-	+0.25	-0.4
22	giss_model_e_h.20c3m.run4	+3.4	-	-	+0.25	-0.7
23	giss_model_e_h.20c3m.run5	+5.9	-	-	+0.31	-0.7
24	giss_model_e_r.20c3m.run1	-0.1	+0. 9	+0.13	+0.18	-0.8
25	giss_model_e_r.20c3m.run2	+4.9	+2.9	+0.13	+0.27	-0.9
26	giss_model_e_r.20c3m.run3	+2.3	+0.1	+0.12	+0.23	-1.1
27	giss_model_e_r.20c3m.run4	-0.1	-0.2	+0.22	+0.39	-0.7
28	giss_model_e_r.20c3m.run5	+0.9	+0.8	+0.20	+0.37	-0.6
29	giss_model_e_r.20c3m.run6	+3.2	+0.1	+0.15	+0.27	-0.8
30	giss_model_e_r.20c3m.run7	+0.6	-0.0	+0.15	+0.34	-0.7
31	giss_model_e_r.20c3m.run8	+2.3	+1.4	+0.18	+0.32	-0.8
32	giss_model_e_r.20c3m.run9	+2.7	+1.5	+0.13	+0.26	-0.9
33	iap_fgoals1_0_g.20c3m.run1	+9.4	+0.5	+0.48	+0.80	+0.8
34	iap_fgoals1_0_g.20c3m.run2	+7.5	-	-	+0.83	+1.2
35	iap_fgoals1_0_g.20c3m.run3	+10.2	-	-	+0.74	+0.7
36	ingv_echam4.20c3m.run1	+2.2	-	+0.53	+0.73	+1.4
37	ipsl_cm4.20c3m.run1	+5.4	-	+0.42	+0.60	+0.9
38	miroc3_2_hires.20c3m.run1	+1.7	-0.4	+0.37	+0.48	-0.1
39	miroc3_2_medres.20c3m.run1	+4.8	+2.3	+0.16	+0.23	-0.5
40	miub_echo_g.20c3m.run1	+0.4	+0.00	+0.13	+0.29	-0.3
41	miub_echo_g.20c3m.run2	+4.4	+2.0	+0.21	+0.32	-0.4

#	Model	Salinity (%PA)	E-P (%PA)	Ocean Temperature (°C)	Global Temperature (°C)	Rainfall (ΔP)
42	miub_echo_g.20c3m.run3	+1.0	+0.2	+0.16	+0.22	-0.5
43	mpi_echam5.20c3m.run1	-	-	-	+0.48	+0.6
44	mpi_echam5.20c3m.run2	-	-	-	+0.24	-0.2
45	mpi_echam5.20c3m.run3	-	-	-	+0.44	+0.9
46	mri_cgcm2_3_2a.20c3m.run1	+3.5	+3.3	-	+0.65	+1.1
47	mri_cgcm2_3_2a.20c3m.run2	+1.9	+3.8	-	+0.62	+1.1
48	mri_cgcm2_3_2a.20c3m.run3	+2.0	+3.3	-	+0.69	+1.5
49	mri_cgcm2_3_2a.20c3m.run4	+1.6	+3.0	-	+0.59	+0.8
50	mri_cgcm2_3_2a.20c3m.run5	+4.2	+4.2	-	+0.63	+1.4
51	ncar_ccsm3_0.20c3m.run1	-	-	-	+0.32	-0.2
52	ncar_ccsm3_0.20c3m.run3	-	-	-	+0.52	+0.2
53	ncar_pcm1.20c3m.run1	-	-	-	-	-
54	ncar_pcm1.20c3m.run3	-	-	-	-	-
55	ncar_pcm1.20c3m.run4	-	-	-	-	-
56	ukmo_hadcm3.20c3m.run1	+0.1	+1.7	-	+0.60	+0.5
57	ukmo_hadcm3.20c3m.run2	+4.7	+4.3	-	+0.67	+0.3
58	ukmo_hadgem1.20c3m.run1	+1.1	+1.3	+0.40	+0.60	+0.2
20C3M Models		20	16	16	23	23
20C3M Simulations		58	47	63	78	73
20C3M De-drifted Simulations		50	44	41	70	68
Ensemble Mean		+3.7	+2.0	+0.33	+0.50	+0.3
Ensemble Standard Deviation		+2.4	+1.8	+0.20	+0.25	+0.9
Observational Estimates		**Salinity (%PA)**	**E-P (%PA)**	**Ocean Temperature (°C)**	**Global Temperature (°C)**	**Rainfall (ΔP)**
Durack & Wijffels (2010; 1950-2000)		+8.0		+0.49		
Boyer *et al.* (2005; 1955-1998)		+5.2				
Wijffels *et al.* (in prep; 1960-2008)				+0.56		
HadCRUT3 (1950-2009)					+0.54	
GISTEMP (1950-2009)					+0.53	
Levitus *et al.* (2009; 1955-2009)				+0.25		
HadSST2 (1950-2009)				+0.37		
HadSST3 (1950-2006)				+0.27		
Kaplan V2 (1950-2009)				+0.24		
ERSST V3b (1950-2009)				+0.31		
OAFlux V3 (1958-2008)			+6.4			
GPCP V2.1 (1979-2008)						-3.7
GPCP V2.2 (1979-2010)						-4.7
CMAP (1979-2008)						-6.0

In order to present the full range of CMIP3 20C3M spatial salinity responses, each of the 58 available model salinity patterns are expressed in Figure S6. These panels show the 1950-2000 mean salinity (top row), the 1950-2000 linear trend (2nd row), the corresponding drift, as captured by a linear trend from the corresponding preindustrial control (PICNTRL) over the years 1900-2049 (3rd row), and the 1950-2000 mean E-P (bottom row).

Figure S6. Ocean salinity amplification is expressed by 23 CMIP3 global climate models in their 20C3M simulations for the period 1950-2000. Top vertical panel represents surface mean salinity for 1950-2000, second vertical panel represents 20C3M surface salinity change for 1950-2000, third vertical panel represents the corresponding PICNTRL drift as determined for 1900-2049 and the lowest vertical panel represents surface mean water flux (E-P) for 1950-2000. Panel numbers represent each model/simulation as numbered in Table S2.

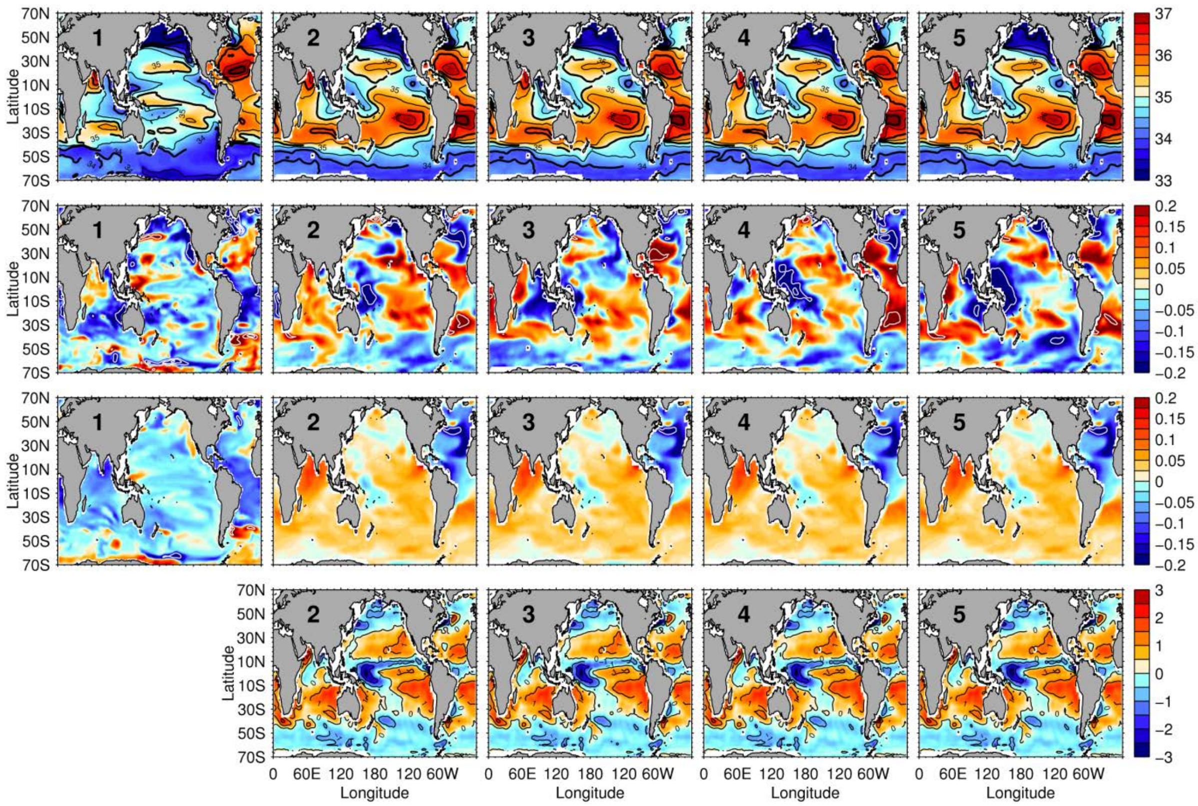

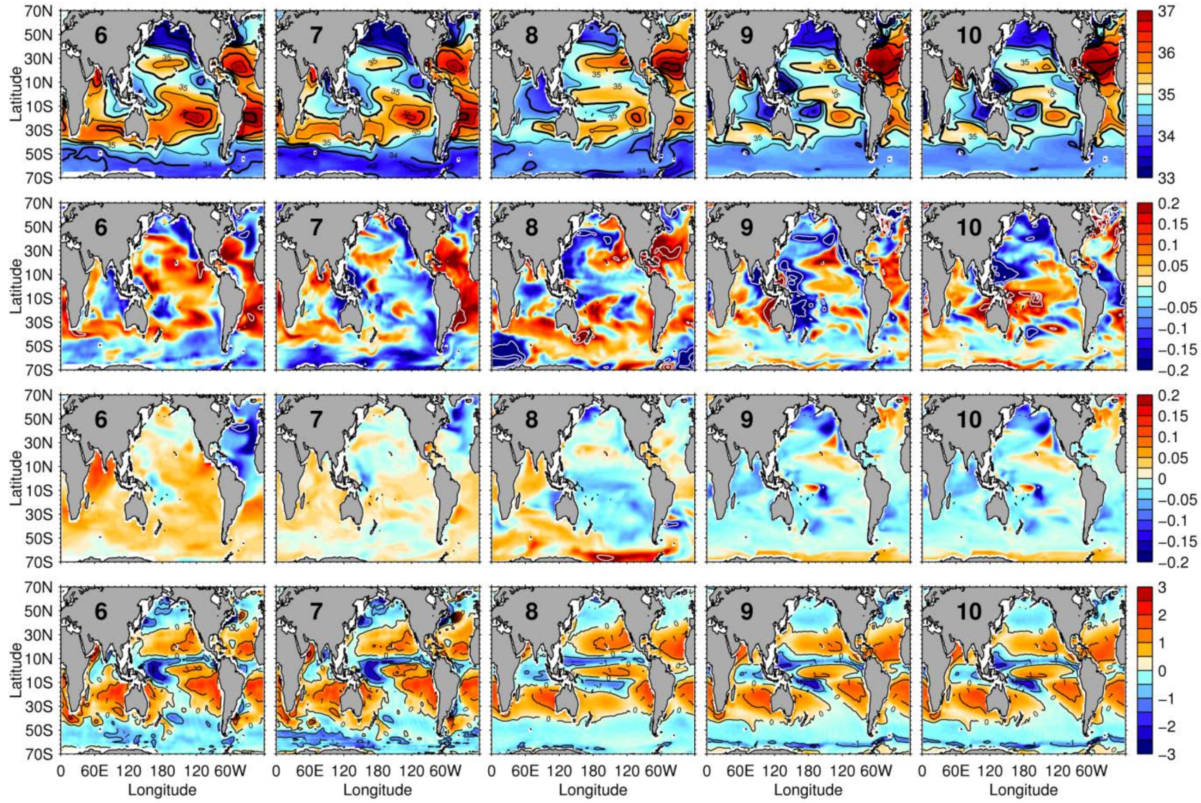

6
7
8
9
10
Latitude
70N
50N
30N
10N
10S
30S
50S
70S
0
60E
120
180
120
60W
Longitude
37
36
35
34
33
0.2
0.15
0.1
0.05
0
−0.05
−0.1
−0.15
−0.2
3
2
1
0
−1
−2
−3

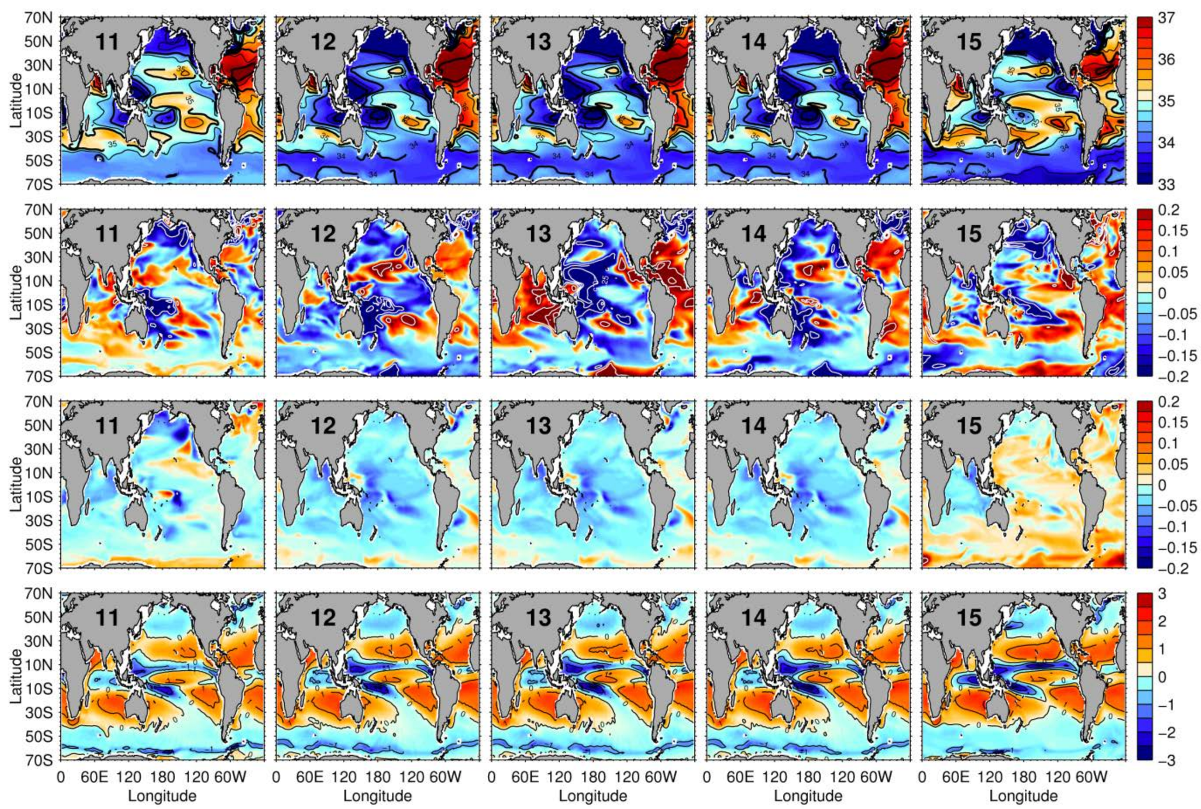

11
12
13
14
15
Latitude
70N
50N
30N
10N
10S
30S
50S
70S
0
60E
120
180
120
60W
Longitude
37
36
35
34
33
0.2
0.15
0.1
0.05
0
−0.05
−0.1
−0.15
−0.2
3
2
1
0
−1
−2
−3

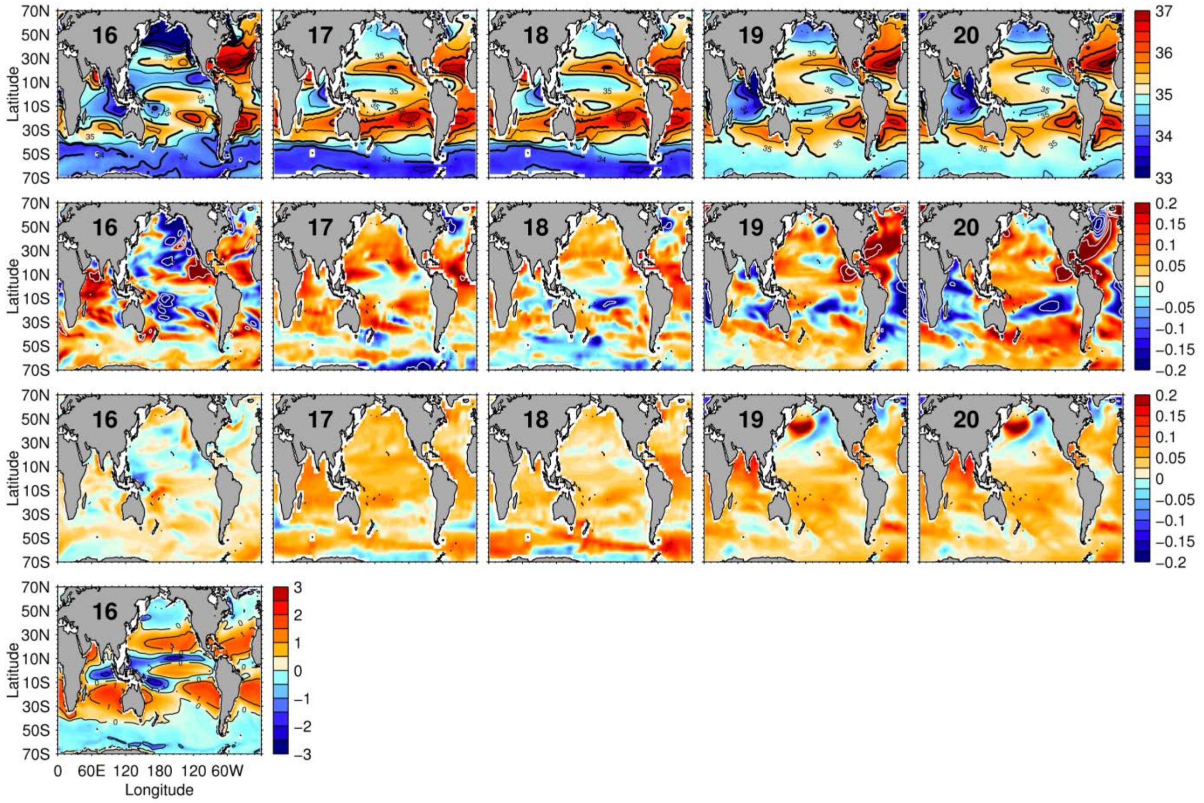
16
17
18
19
20
Latitude
Longitude
70N 50N 30N 10N 10S 30S 50S 70S
0 60E 120 180 120 60W
37 36 35 34 33
0.2 0.15 0.1 0.05 0 −0.05 −0.1 −0.15 −0.2
3 2 1 0 −1 −2 −3

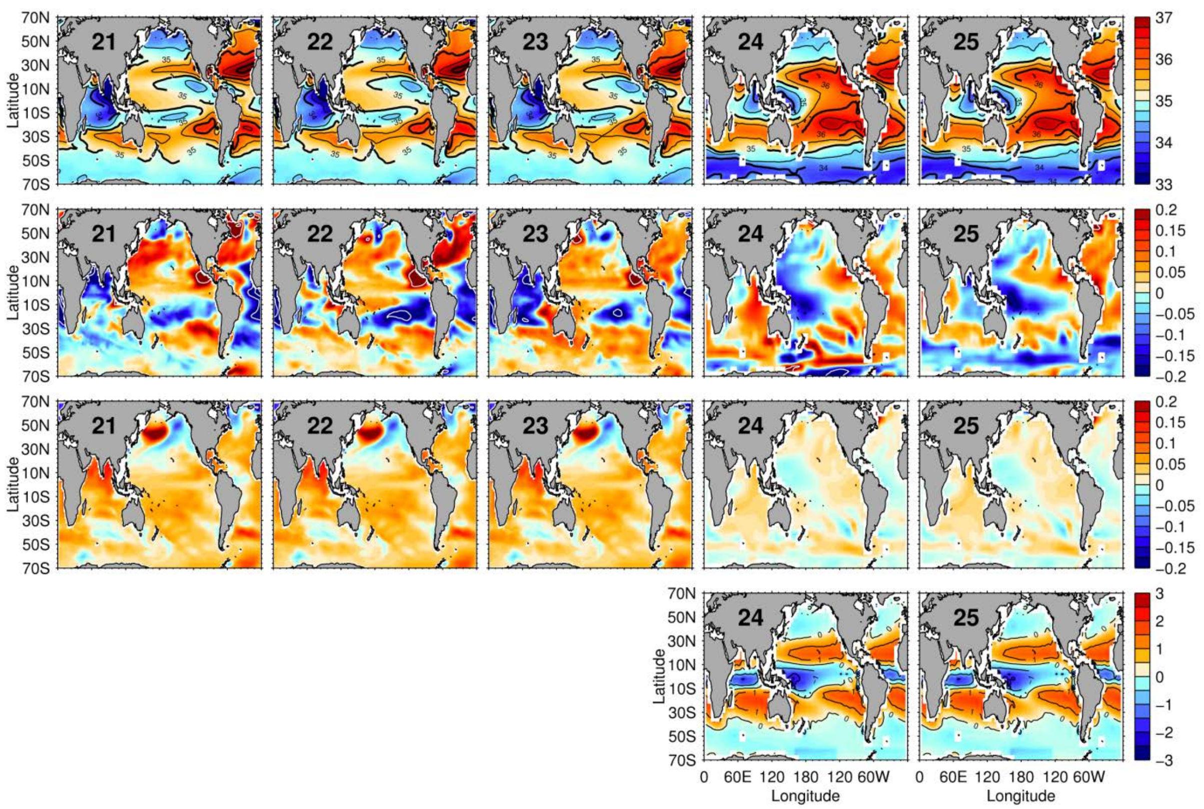
21
22
23
24
25
Latitude
Longitude
70N 50N 30N 10N 10S 30S 50S 70S
0 60E 120 180 120 60W
37 36 35 34 33
0.2 0.15 0.1 0.05 0 −0.05 −0.1 −0.15 −0.2
3 2 1 0 −1 −2 −3

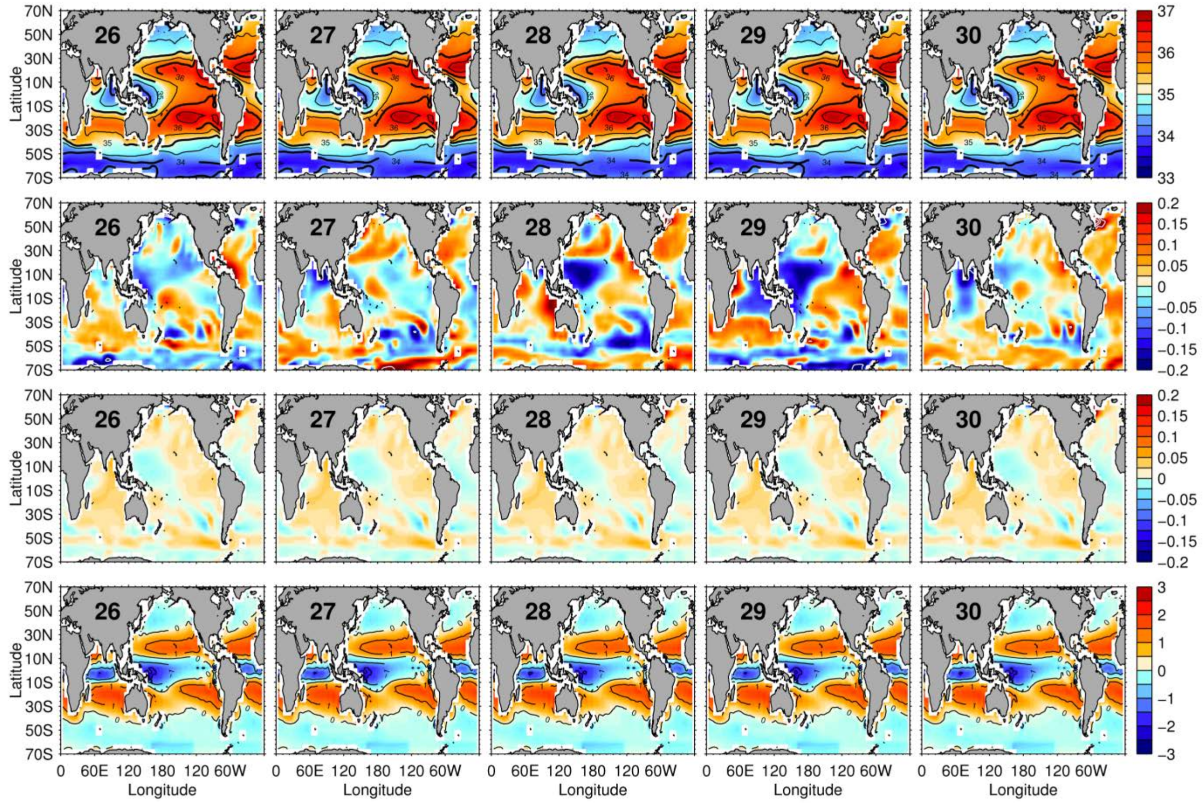
26
27
28
29
30
Latitude
Longitude
70N 50N 30N 10N 10S 30S 50S 70S
0 60E 120 180 120 60W
37 36 35 34 33
0.2 0.15 0.1 0.05 0 −0.05 −0.1 −0.15 −0.2
3 2 1 0 −1 −2 −3

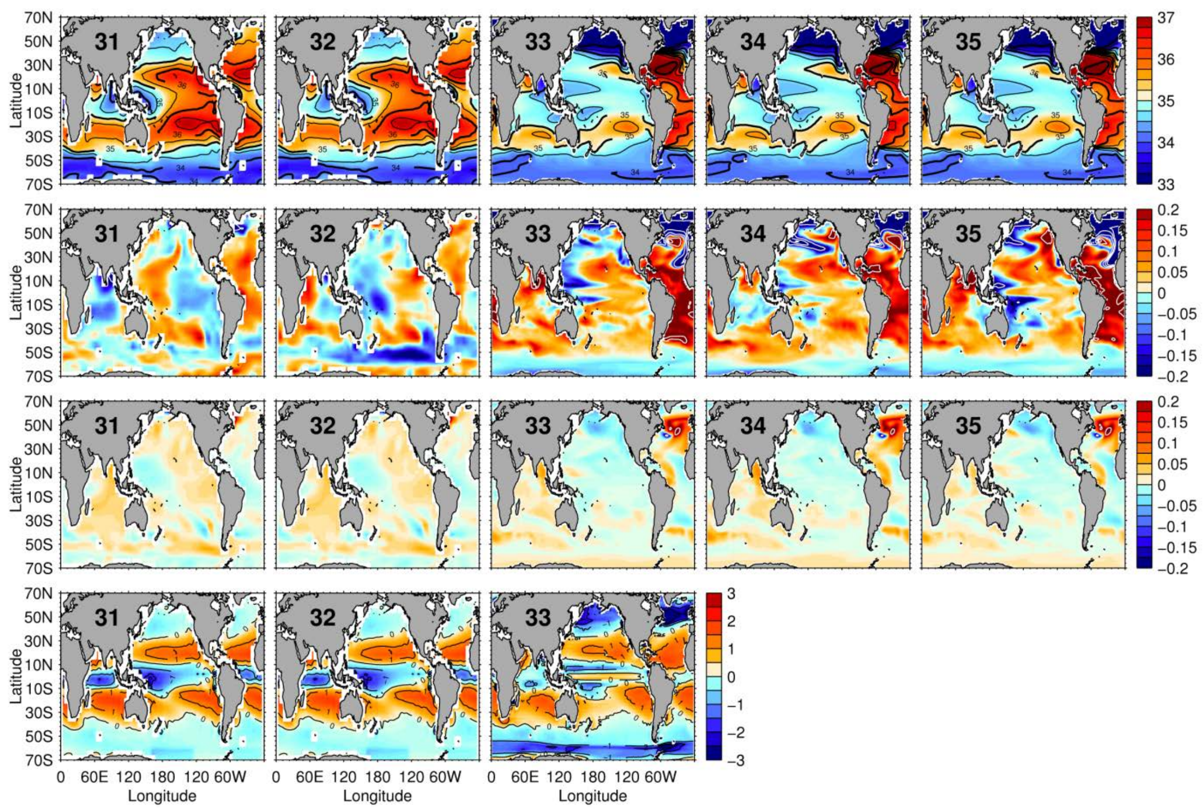
31
32
33
34
35
Latitude
Longitude
70N 50N 30N 10N 10S 30S 50S 70S
0 60E 120 180 120 60W
37 36 35 34 33
0.2 0.15 0.1 0.05 0 −0.05 −0.1 −0.15 −0.2
3 2 1 0 −1 −2 −3

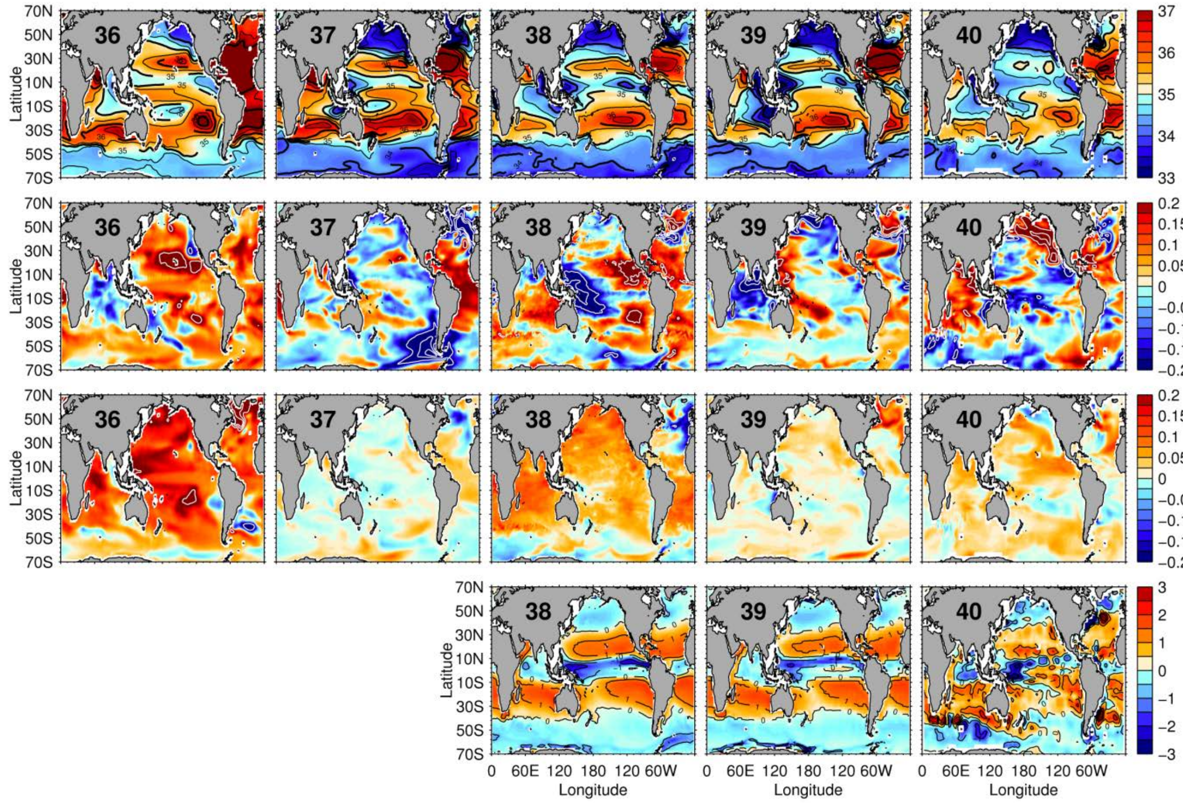
36
37
38
39
40
70N 50N 30N 10N 10S 30S 50S 70S
Latitude
0 60E 120 180 120 60W
Longitude
37 36 35 34 33
0.2 0.15 0.1 0.05 0 −0.05 −0.1 −0.15 −0.2
3 2 1 0 −1 −2 −3

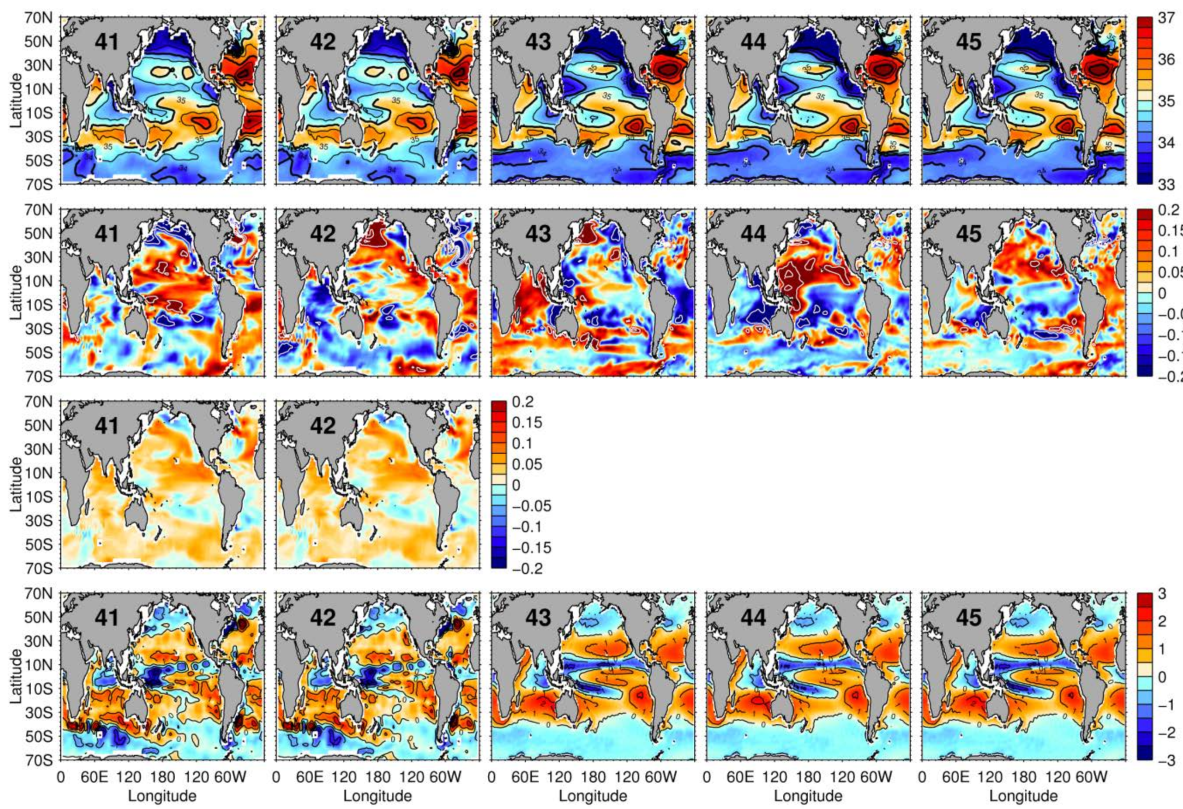
41
42
43
44
45
70N 50N 30N 10N 10S 30S 50S 70S
Latitude
0 60E 120 180 120 60W
Longitude
37 36 35 34 33
0.2 0.15 0.1 0.05 0 −0.05 −0.1 −0.15 −0.2
3 2 1 0 −1 −2 −3

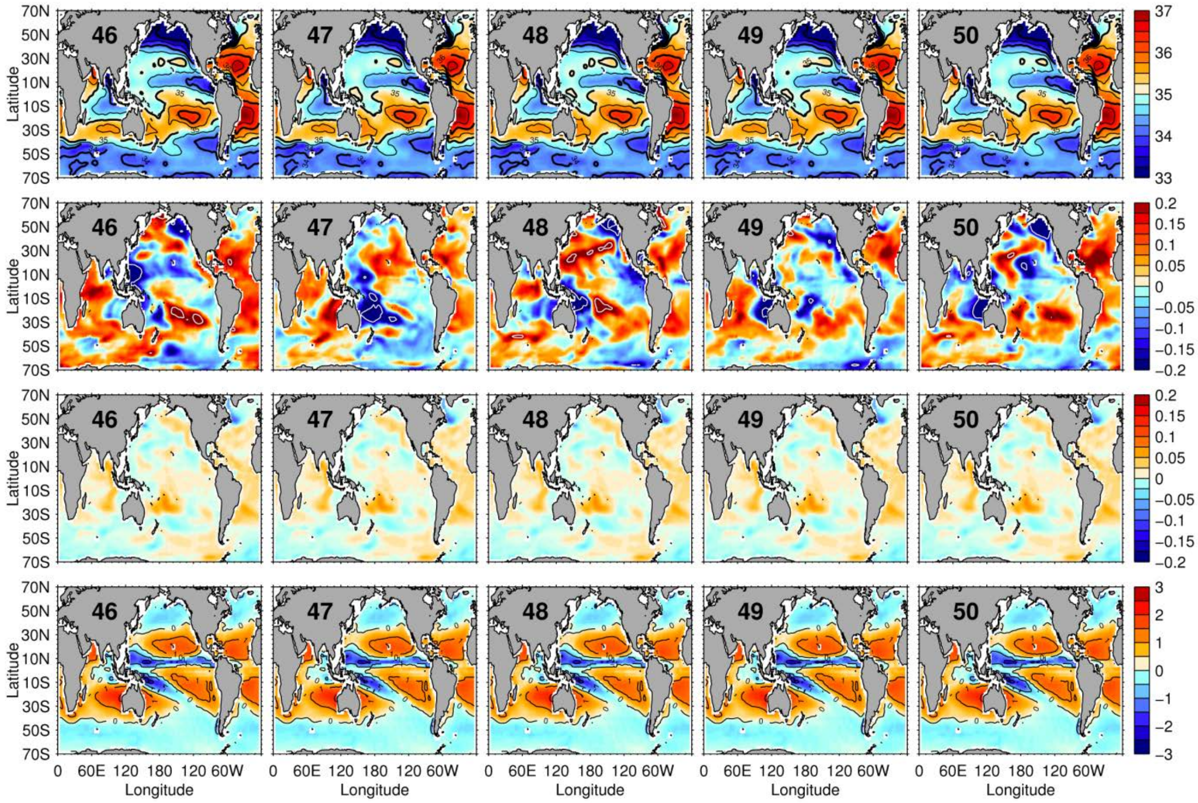
46
47
48
49
50
70N
50N
30N
10N
10S
30S
50S
70S
Latitude
0
60E
120
180
120
60W
Longitude
37
36
35
34
33
0.2
0.15
0.1
0.05
0
−0.05
−0.1
−0.15
−0.2
3
2
1
0
−1
−2
−3

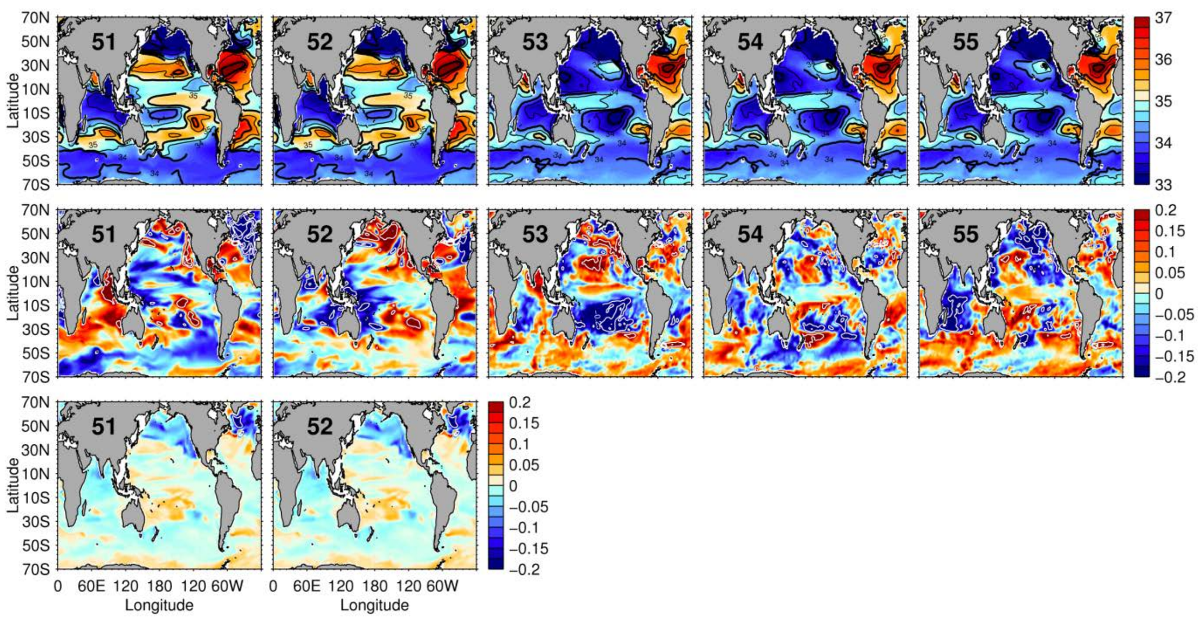
51
52
53
54
55
70N
50N
30N
10N
10S
30S
50S
70S
Latitude
0
60E
120
180
120
60W
Longitude
37
36
35
34
33
0.2
0.15
0.1
0.05
0
−0.05
−0.1
−0.15
−0.2

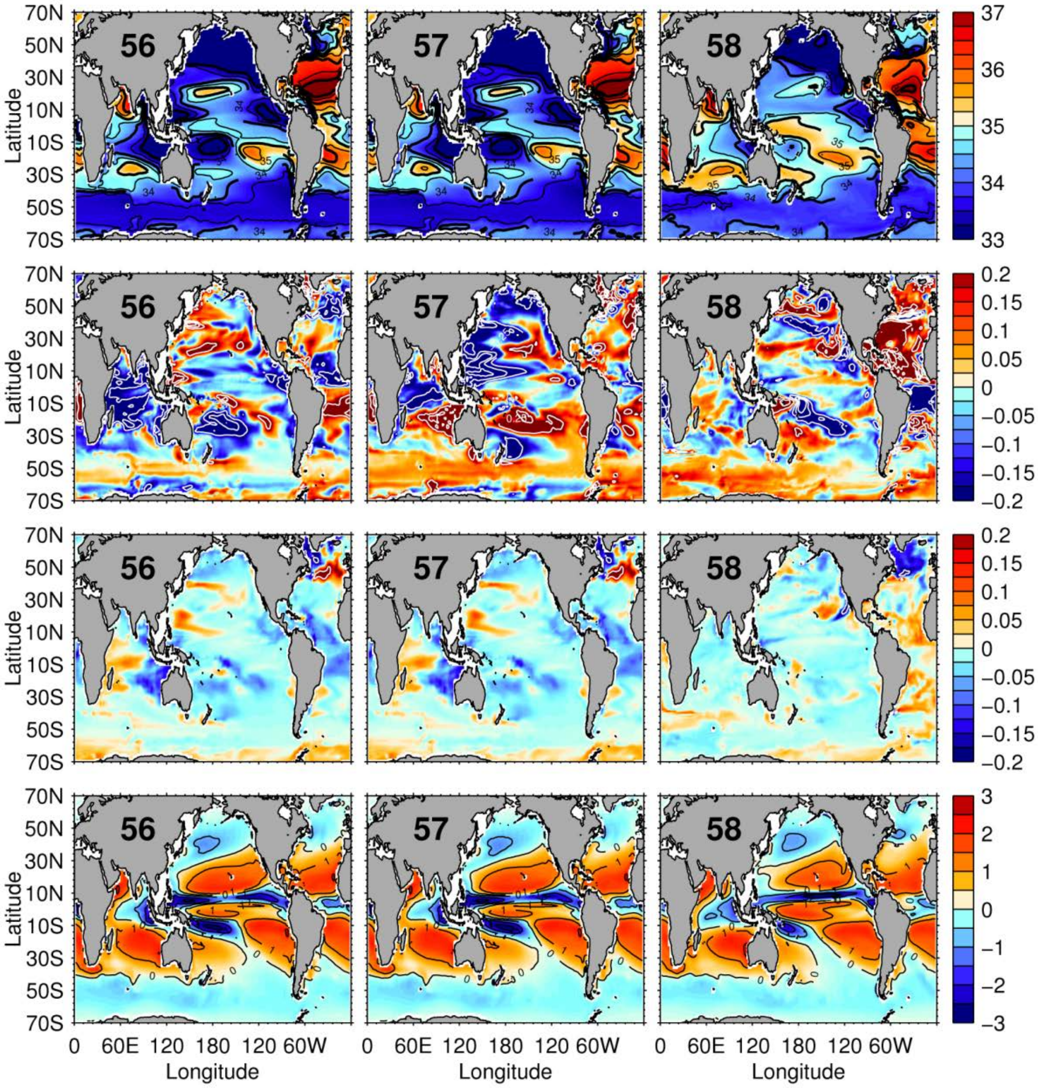

56
57
58
Latitude
Longitude
70N
50N
30N
10N
10S
30S
50S
70S
0
60E
120
180
120
60W
37
36
35
34
33
0.2
0.15
0.1
0.05
0
−0.05
−0.1
−0.15
−0.2
3
2
1
0
−1
−2
−3

Idealised Ocean-model Experiments

For this experiment we used a version of the MOM3 ocean model (Matear & Lenton, 2008), which was forced with surface water flux fields obtained from the NCEP reanalysis. These experiments were constructed to test the salinity response to an idealised, linearly increasing E-P forcing over an equivalent time period to the observational salinity analysis (1950-2000). The model was spun-up over the representative years 1850 to 1948 with daily surface fluxes. The ocean was initialised using the climatological fields of temperature and salinity from the World Ocean Atlas 2001 (Conkright *et al*., 2002). In order to minimise modelled climate variability and enhance the spatial change signal in the idealised runs, a single year (1948) from the NCEP-1 reanalysis (Kalnay *et al*., 1996) was selected. This data then provided the daily surface forcing fields; wind stresses, heat and water fluxes, which were perennially applied to the ocean model. These 1948 annual fluxes were then used for the model spin-up, 1850-1948 with both sea surface temperature (SST; Reynolds & Smith, 1994) and salinity (Conkright *et al*., 2002) restored to annual climatologies on a 30-day timescale. For the idealised runs, and the corresponding control run (which extended from 1948-2009), salinity restoring was not undertaken, however SST restoring was enabled. In plots presented in Figure S7 & S8 we show the salinity change with the control run drift removed, with the difference attributable to the idealised surface E-P forcing.

Linear increasing trends to surface water fluxes were imposed over the 1948-2009 period. To attempt to capture the range of linear and non-linear responses to such surface water flux changes, runs imposed with a 5%, 10%, 15% and 20% E-P change were undertaken, additional to a control with no changes to surface water fluxes. These model runs were then investigated for their surface (and subsurface) salinity changes, and compared to the comparative 1950-2000 observed patterns of salinity change.

Each of the model runs (Figure S7C, D, E, F) express the surface salinity response for the 50-year period over which the linear increasing trend to E-P was imposed, with the corresponding control drift removed point-wise from each representative field. These idealised runs tend to replicate the broad-scale patterns of the observational analysis (Figure S7A). A coherent freshening of the Pacific is apparent, with the exception of a zonal enhancement to surface salinities located along the subtropical salinity maxima, broadly following the E-P maxima of the basin. In the Atlantic, strong surface salinity increases are apparent aligned with the subtropical salinity maxima in both the North and South Atlantic. In the Indian, an enhanced salinity is found in the Arabian Sea, with a strong freshening in the Bay of Bengal. The enhanced salinity, associated with the subtropical salinity maxima is much broader in observations when compared to the idealised model results.

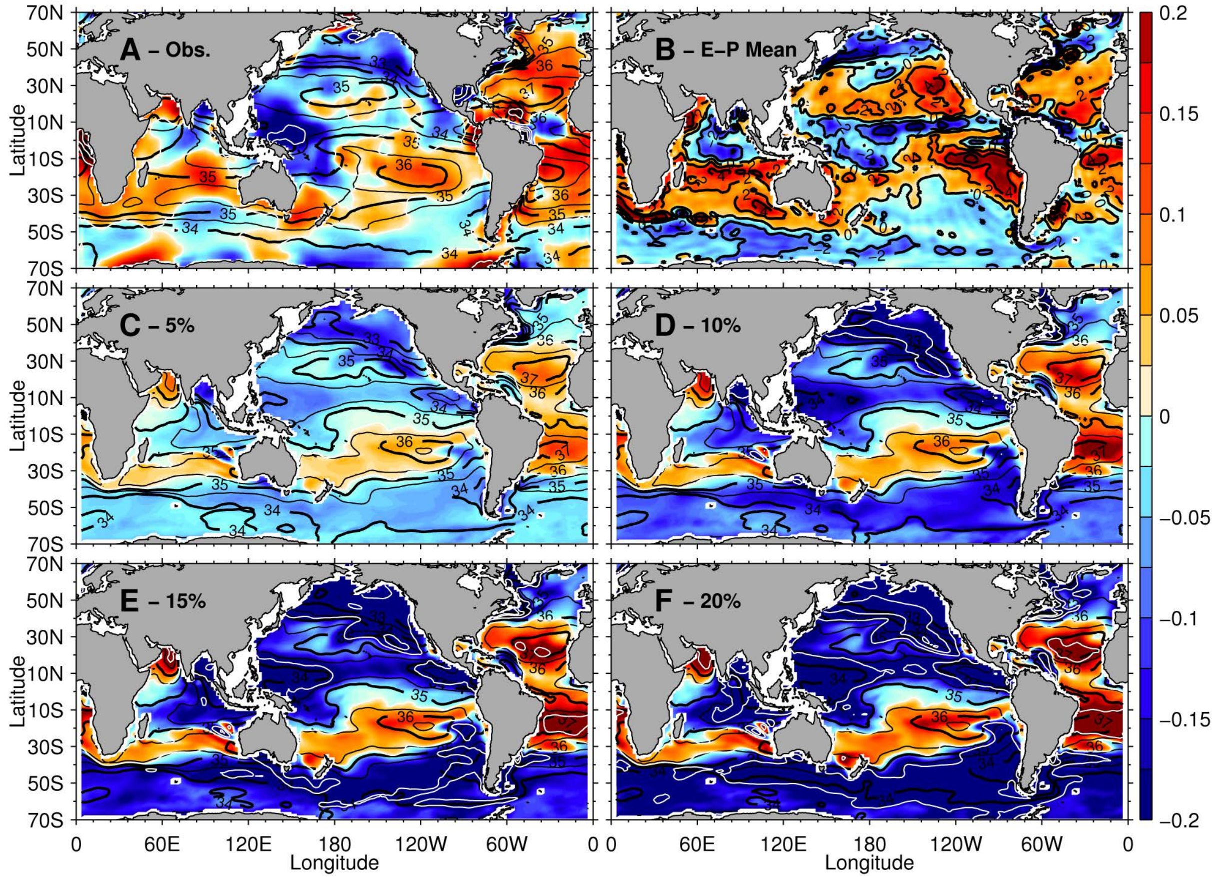

Figure S7. Patterns of 50-year surface salinity change (PSS-78 50 yr^{-1}). A) The 1950-2000 observational result of Durack & Wijffels (2010). B) The climatological annual mean surface water flux (m yr^{-1}) as obtained from NCEP-1 (Kalnay *et al.*, 1996). The idealised surface salinity response for a: C) 5%, D) 10%, E) 15% and F) 20% surface water flux enhancement over 50 years. For each panel, the corresponding mean salinity is contoured in black, with thick lines every 1 (PSS-78) and thin lines every 0.5 (PSS-78).

Additional to a surface salinity comparison, global subsurface zonal mean comparison was also undertaken (Figure S8). A strong coherence is found between the observed result (Figure S8A) and those of the idealised simulations. In these simulations the salty southern subtropical gyre bowl is expressing a strong enhanced salinity, whereas the Northern Hemisphere response is less coherent. The high latitude freshening is also captured in this model, however the subduction of this signal into the ocean interior is weaker than in observations, particularly in the Southern Hemisphere. This feature is most clear when comparing the climatological salinity (contoured) with a deep and clear salinity minima tongue visible extending to 1500 dbar in observations (Figure S8A), with this feature noticeably absent in the model (Figure S8B-E). The independent basin changes (not shown) provide even stronger evidence that regional basin-wide salinity changes, reported in observations are linked to E-P changes at the surface. We note that this model does not provide a perfect replication of the global ocean structure, with a weaker salinity minima subduction and circulation pathway into the deep interior when compared to our observational understanding (contrast S8A vs B, C, D, E). This would then lead to difficulties in interpreting deeper ocean changes on longer timescales (> 50-years) as the model replication of such deep ocean interior changes are likely to be muted when compared to observations.

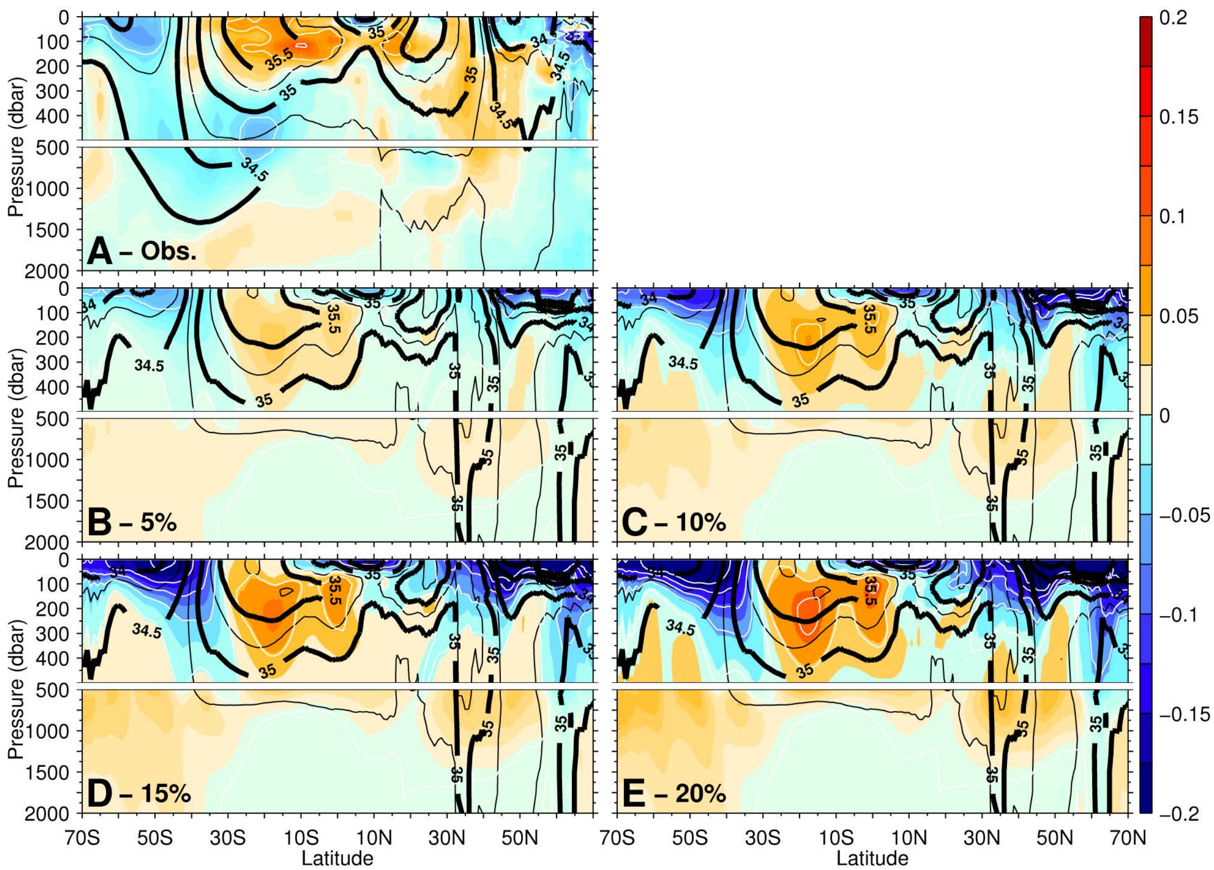

Figure S8. Patterns of 50-year subsurface zonal mean salinity change (PSS-78 50 yr^{-1}). A) The 1950-2000 observational result of Durack & Wijffels (2010). The idealised subsurface salinity response for a: B) 5%, C) 10%, D) 15% and E) 20% surface water flux enhancement over 50 years. For each panel, the corresponding mean salinity is contoured in black, with thick lines every 0.5 (PSS-78) and thin lines every 0.25 (PSS-78).

When comparing these idealised model simulations to those of the CMIP3 suite it is clear that this ocean-only simulation underestimates the CMIP3 1:2 relationship between E-P PA and SSS PA (not shown, with a value near 1:1). Three reasons for these differences may include:

1) A link exists between ocean warming and the SSS trend which amplifies the resolved SSS PA
2) Net sea-ice melt in the CMIP3 simulations provides an additional freshwater source term which is not included in the idealised ocean-only simulations
3) Terrestrial storage changes as captured by CMIP3 changes the relationship

Some preliminary investigations suggest that ocean warming when coupled with the idealised E-P forcing does increase the SSS PA – this is possibly linked to increasing ocean stratification, where a smaller control volume is experiencing the effects of the E-P forcing. Some CMIP3 analyses (Russell *et* al., 2006; Luo *et al.*, 2009; Joo Jang *et al*., 2011) suggest such stratification changes will occur due to climate change, however, dynamically these changes are complex (Russell *et* al., 2006). Changes to terrestrial E-P and the resulting runoff is another potential source of ocean change with more regional effects likely, however such effects are not captured in the idealised ocean-only simulations. The reduction in summer sea-ice in CMIP3 projections, particularly in the Arctic (e.g. Zhang & Walsh, 2006; Wang & Overland, 2009) could also drive strong change, with large SSS declines in the high latitudes suggesting this process may be operating – we note again however that dynamic ice processes are not included in these idealised ocean-only simulations.

The lack of these 3 processes in the idealised ocean-only simulations makes the CMIP3 simulations a better choice in which to calibrate the E-P PA and SSS PA.

Observational Estimates of Water Cycle Change

Estimates of water cycle change have been obtained from numerous observational and satellite-based platforms. How do resolved changes from differing observed platforms compare to the new water cycle change estimate expressed by ocean salinity from 1950-2000? In Figure S9 we compile observed water cycle change estimates from many selected studies, with each of these expressing the explicit rate of water cycle rate per degree of global surface warming over the corresponding period of analysis, obtained from HadCRUT3 (Brohan *et al*., 2006).

It is clear when reviewing the comparative results presented in Figure S8 that a large portion of these observed estimates suggest that a water cycle response on or near Clausius-Clapeyron (7% $°C^{-1}$) is apparent. It is also clear that no matter which CMIP3 ensemble mean estimate is utilised (salinity, E-P or global mean rainfall), these tend to provide conservative estimates of such changes when compared to the available observational comparisons.

Many of the presented atmospheric estimates provide trends obtained over periods less than 30-years, and so decadal climate variability may strongly influence such short-term trends. Additionally, the use of satellite data from numerous independent missions ensures that difficulties with cross-mission calibration can strongly influence the magnitude and sign of the resolved trends (see main text).

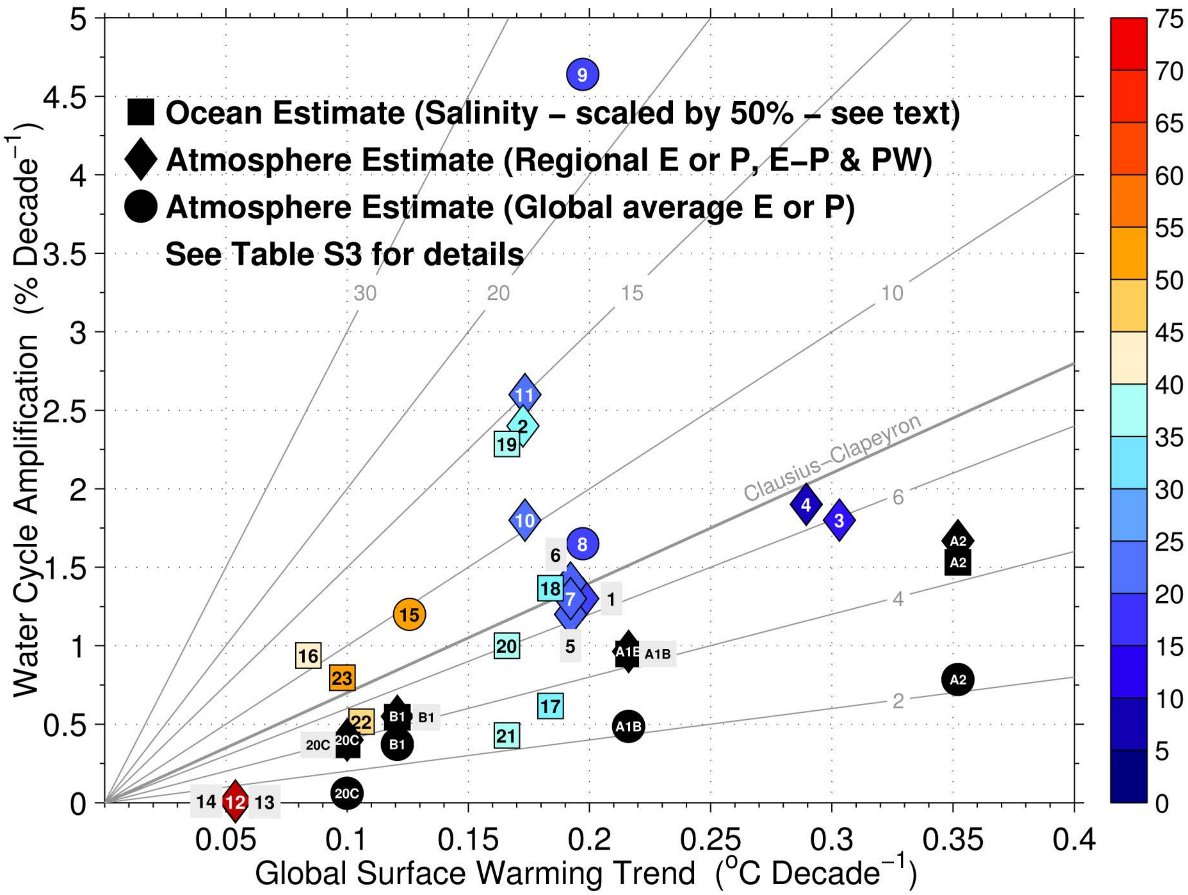

Figure S9. Reported observed water cycle changes (scaled in relative absolute change decade^{-1}). Colours indicate years over which reported changes are calculated (red is longer). As noted in the figure, ocean salinity estimates are presented as squares (scaled by 50% of their reported magnitudes to represent equivalent E-P change as obtained from the CMIP3 ensemble relationship, see text), atmospheric water cycling estimates (non-average global rainfall/evaporation) are triangles and average global rainfall/evaporation are circles. All ΔTa trends were obtained from HadCRUT3 (Brohan *et al.*, 2006) using a linear fit over the corresponding years (annual data) used to determine the water cycle change estimate. More detail, including error estimates for each of the noted studies is contained in Table S1. The result suggested by this study is #23. For reference, equivalent scenario ensemble mean changes for the 20C3M (1950-2000; 20C) and SRES (2050-2099; B1, A1B, A2) simulations are included in black. Grey lines express constant proportional change; line representing Clausius-Clapeyron (CC) is 7% °C^{-1}. A total of 14 independent studies and 23 estimates of global and regional changes which express different aspects of water cycle change are presented.

Table S3: Some representative observed water cycle changes for the 20^{th} and early 21^{st} century, as expressed in Figure S8. Salinity estimates are scaled by 50% (in Figure S9; unscaled salinity values are expressed below) to represent E-P changes using the relationship obtained from the CMIP3 model suite (see main text). All global warming trends were obtained from HadCRUT3 (Brohan *et al*., 2006) as a linear trend over the period of analysis, following the MetOffice smoothed annual average temperature technique described at http://hadobs.metoffice.com/hadcrut3/smoothing.html (accessed 13th July 2011). Error estimates in the last column indicate formal errors resolved from the linear warming trend combined with water cycle error bounds (if available). Estimates are presented at 99% confidence for the warming plus the water cycle error.

	Author	Instrument	Region	Period	Change per Decade	Change per K
1	Trenberth *et al.*, 2005	SSM/I	Global PW	1987-2004	1.3±0.3%	7±16% K^{-1}
2	Durre *et al.*, 2009	Radiosondes	Northern Hemisphere PW	1973-2006	2.4%	14% K^{-1}
3	Keihm *et al.*, 2009	TMR	global PW 60°S-60°N	1992-2005	1.8±0.4%	6±9% K^{-1}
4	Mieruch *et al.*, 2008	GOME & SCIAMACHY	Global PW	1996-2002	1.9±0.7%	7±4% K^{-1}
5	Wentz *et al.*, 2007	SSM/I	Tropical PW	1987-2006	1.2±0.4%	6±11% K^{-1}
6	Wentz *et al.*, 2007	SSM/I	Tropical P	1987-2006	1.4±0.5%	7±14% K^{-1}
7	Wentz *et al.*, 2007	SSM/I	Tropical E	1987-2006	1.3±0.5%	7±13% K^{-1}
8	Liepert & Previdi, 2009	OAFlux	Global Ocean E	1987-2004	1.6±0.8%	8±27% K^{-1}
9	Liepert & Previdi, 2009	HOAPS	Global Ocean E	1987-2004	4.6±3.6%	24±95% K^{-1}
10	Allan *et al.*, 2010	GPCP_V2.1/SSM/I	Tropical Hi-P	1988-2008	1.8±0.5%	10±23% K^{-1}
11	Allan *et al.*, 2010	GPCP_V2.1/SSM/I	Tropical Lo-P	1988-2008	-2.6±0.8%	-15±9% K^{-1}
12	Zhang *et al.*, 2007	GHCN	Land P 30°S-0	1925-1999	0.006%	<1% K^{-1}
13	Zhang *et al.*, 2007	GHCN	Land P 0-30°N	1925-1999	-0.007%	<1% K^{-1}
14	Zhang *et al.*, 2007	GHCN	Land P 40-70°N	1925-1999	0.01%	<1% K^{-1}
15	Yu, 2007 (updated)	OAFlux_V3	Global Ocean E	1958-2008	1.2±0.5%	10±8% K^{-1}
16	Curry *et al.*, 2003	Ocean profile data	E-P inferred (Atlantic salinity)	1950-1990	1.9% (5-10)	22% K^{-1}
17	Hosoda *et al.*, 2009	Ocean profile data	E-P inferred (Global salinity)	1974-2005	1.2±1.5%	7±14% K^{-1}
18	Hosoda *et al.*, 2009	Ocean profile data	E-P inferred (Southern Ocean salinity)	1974-2005	2.7±2.1%	15±22% K^{-1}
19	Helm *et al.*, 2010	Ocean profile data	E-P inferred (Southern Ocean salinity)	1970-2005	4.6±1.7%	28±25% K^{-1}
20	Helm *et al.*, 2010	Ocean profile data	E-P inferred (Northern Hemisphere Hi-latitude salinity)	1970-2005	2.0±1.1%	12±14% K^{-1}
21	Helm *et al.*, 2010	Ocean profile data	E-P inferred (Subtropical gyres salinity)	1970-2005	-0.9±0.6%	-5±4% K^{-1}
22	Boyer *et al.*, 2005	Ocean profile data	Global Ocean surface salinity	1955-1998	1.0±0.1%	10±7% K^{-1}
23	This study	Ocean profile data	Global Ocean surface salinity	1950-2000	1.6±0.1%	16±7% K^{-1}
-	This study	Ocean profile data	Pacific Ocean surface salinity	1950-2000	1.4±0.1%	15±7% K^{-1}
-	This study	Ocean profile data	Atlantic Ocean surface salinity	1950-2000	1.4±0.1%	15±7% K^{-1}
-	This study	Ocean profile data	Indian Ocean surface salinity	1950-2000	1.2±0.1%	12±7% K^{-1}

References and Notes

Allan, R.P., B.J. Soden, V.O. John, W. Ingram and P. Good (2010) Current changes in tropical precipitation. *Environmental Research Letters*, **5**, 025205. doi: 10.1088/1748-9326/5/2/025205

Baumgartner, A. and E. Reichel (1975) *The World Water Balance: Mean Annual Global, Continental and Maritime Precipitation, Evaporation and Runoff*. Elsevier Science Ltd. Amsterdam. 179 pp

Boyer, T.P., S. Levitus, J.I. Antonov, R.A. Locarnini and H.E. Garcia (2005) Linear trends in salinity for the World Ocean, 1955-1998. *Geophysical Research Letters*, **32**, L01604. doi: 10.1029/2004GL021791

Brohan, P., J.J. Kennedy, I. Harris, S.F.B. Tett and P.D. Jones (2006) Uncertainty estimates in regional and global observed temperature changes: A new data set from 1850. *Journal of Geophysical Research*, **111**, D12106. doi: 10.1029/2005JD006548

Chen, G., Y. Ming, N.D. Singer and J. Lu (2011) Testing the Clausius-Clapeyron constraint on the aerosol-induced changes in mean and extreme precipitation. *Geophysical Research Letters*, **38**, L04807. doi: 10.1029/2010GL046435

Conkright, M.E., R.A. Locarnini, H.E. Garcia, T.D. O'Brien, T.P. Boyer, C. Stephens and J.I. Antonov (2002) World Ocean Atlas 2011: Objective Analyses, Data Statistics and Figures, CD-ROM Documentation. NODC Internal Report 17, 17 pp

Curry, R., B. Dickson and I. Yashayaev (2003) A change in the freshwater balance of the Atlantic Ocean over the past four decades. *Nature*, **426**, pp 826-829. doi: 10.1038/nature02206

Durack, P.J. and S.E. Wijffels (2010) Fifty-Year Trends in Global Ocean Salinities and Their Relationship to Broad-Scale Warming. *Journal of Climate*, **23**, pp 4342-4362. doi: 10.1175/2010JCLI3377.1

Durack, P.J., S.E. Wijffels and N.L. Bindoff (2011) [Global Oceans] Ocean Salinity: A Water Cycle Diagnostic? [In "State of the Climate 2010"], *Bulletin of the American Meteorological Society*, **92** (6), S91-S93. doi: 10.1175/BAMS-92-6-StateoftheClimate

Durre, I., C.N. Williams Jr, X. Yin and R.S. Vose (2009) Radiosonde-based trends in precipitable water over the Northern Hemisphere: An update. *Journal of Geophysical Research*, **114**, D05112. doi: 10.1029/2008JD010989

Helm, K.P., N.L. Bindoff and J.A. Church (2010) Changes in the global hydrological-cycle inferred from ocean salinity. *Geophysical Research Letters*, **37**, L18701. doi: 10.1029/2010GL044222

Hosoda, S., T. Sugo, N. Shikama and K. Mizuno (2009) Global Surface Layer Salinity Change Detected by Argo and Its Implication for Hydrological Cycle Intensification. *Journal of Oceanography*, **65**, pp 579-586

Joo Jang, C., J. Park, T. Park and S. Yoo (2011) Response of the ocean mixed layer depth to global warming and its impact on primary production: a case for the North Pacific Ocean. *ICES Journal of Marine Science*, **68**, pp 996-1007. doi: 10.1093/icesjms/fsr064

Kalnay, E., M. Kanamitsu, R. Kistler, W. Collins, D. Deaven, L. Gandin, M. Iredell, S. Saha, G. White, J. Woollen, Y. Zhu, A. Leetmaa and R. Reynolds (1996) The NCEP/NCAR 40-Year Reanalysis Project. *Bulletin of the American Meteorological Society*, **77**, pp 437-473. doi: 10.1175/1520-0477(1996)077<0437:TNYRP>2.0.CO;2

Keihm, S., S. Brown, J. Teixeira, S. Desai, W. Lu, E. Fetzer, C. Ruf, X. Huang and Y. Yung (2009) Ocean water vapor and cloud liquid water trends from 1992 to 2005 TOPEX Microwave Radiometer data. *Journal of Geophysical Research*, **114**, D18101. doi: 10.1029/2009JD012145

Levitus, S. J.I. Antonov, T.P. Boyer, R.A. Locarnini, H.E. Garcia and A.V Mishonov (2009) Global ocean heat content 1955-2008 in light of recently revealed instrumentation problems. *Geophysical Research Letters*, **36**, L070608. doi: 10.1029/2008GL037155

Liepert, B.G. and M. Previdi (2009) Do Models and Observations Disagree on the Rainfall Response to Global Warming? *Journal of Climate*, **22**, pp 3156-3166. doi: 10.1175/2008JCLI2472.1

Luo, Y., Q. Liu ad L.M. Rothstein (2009) Simulated response of North Pacific Mode Waters to global warming. *Geophysical Research Letters*, **36**, L23609. doi: 10.1029/2009GL040906

Matear, R.J. and A. Lenton (2008) Impact of Historical Climate Change on the Southern Ocean Carbon Cycle. *Journal of Climate*, **21**, pp 5820-5834. doi: 10.1175/2008JCLI2194.1

Mieruch, S., S. Noël, H. Bovensmann and J.P. Burrows (2008) Analysis of global water vapour trends from satellite measurements in the visible spectral range. *Atmospheric Chemistry and Physics*, **8**, pp 491-504. doi: 10.5194/acp-8-491-2008

Ming, Y., V. Ramaswamy and G. Persad (2010) Two opposing effects of absorbing aerosols on global-mean precipitation. *Geophysical Research Letters*, **37**, L13701. doi: 10.1029/2010GL042895

Ramanathan, V., P.J. Crutzen, J.T. Kiehl and D. Rosenfeld (2001) Aerosols, Climate, and the Hydrological Cycle. *Science*, **294**, pp 2119-2124. doi: 10.1126/science.1064034

Reynolds, R.W. and T.M. Smith (1994) Improved Global Sea Surface Temperature Analyses Using Optimal Interpolation. *Journal of Climate*, **7**, pp 929-948. doi: 10.1175/1520-0442(1994)007<0929:IGSSTA>2.0.CO;2

Russell, J.L., K.W. Dixon, A. Gnanadesikan, R.J. Stouffer and J.R. Toggweiler (2006) The Southern Hemisphere Westerlies in a Warming World: Propping Open the Door to the Deep Ocean. *Journal of Climate*, **19**, pp 6382-6390. doi: 10.1175/JCLI3984.1

Santer, B.D., C. Mears, F.J. Wentz, K.E. Taylor, P.J. Gleckler, T.M.L. Wigley, T.P. Barnett, J.S. Boyle, W. Bruggemann, N.P. Gillett, S.A. Klein, G.A. Meehl, T. Nozawa, D.W. Pierce, P.A. Stott, W.M Washington and M.F. Wehner (2007) Identification of human-induced changes in atmospheric moisture content. *Proceedings of the National Academy of Sciences*, **104**, pp 15248-15253. doi: 10.1073/pnas.0702872104

Schanze, J.J., R.W. Schmitt and L.L. Yu (2010) The Global Oceanic Freshwater Cycle: A Best-Estimate Quantification. *Journal of Marine Research*, **68**, pp 569-595. doi: 10.1357/002224010794657164

Schmitt, R.W. (1995) The ocean component of the global water cycle. U.S. National Report to the International Union of Geodesy and Geophysics, 1991-1994. *Reviews of Geophysics*, **33** (Supplement), pp 1395-1409

Trenberth, K.E., J. Fasullo and L. Smith (2005) Trends and variability in column-integrated atmospheric water vapor. *Climate Dynamics*, **24**, pp 741-758. doi: 10.1007/s00382-005-0017-4

Trenberth, K.E., L. Smith, Q. Taotao, A. Dai and J. Fasullo (2007) Estimates of the Global Water Budget and Its Annual Cycle Using Observational and Model Data. *Journal of Hydrometeorology*, **8**, pp 758-769. doi: 10.1175/jhm600.1

Wentz, F.J., L. Ricciardulli, K. Hilburn and C. Mears (2007) How Much More Rain Will Global Warming Bring? *Science*, **317**, pp 233-235. doi: 10.1126/science.1140746

Yu, L. (2007) Global Variations in Oceanic Evaporation (1958-2005): The Role of the Changing Wind Speed. *Journal of Climate*, **20**, pp 5376-5390. doi: 10.1175/2007JCLI1714.1

Wang, M. and J.E. Overland (2009) A sea ice free summer Arctic within 30 years? *Geophysical Research Letters*, **36**, L07502. doi: 10.1029/2009GL037820

Wijffels, S.E. et al. (in prep) Detection and Anatomy of Linear Ocean Warming from 1960 to 2010

Zhang, X. and J.E. Walsh (2006) Toward a Seasonally Ice-Covered Arctic Ocean: Scenarios from the IPCC AR4 Model Simulations. *Journal of Climate*, **19**, pp 1730-1747. doi: 10.1175/JCLI3767.1

Zhang, X., F.W. Zwiers, G.C. Hegerl, F.H. Lambert, N.P. Gillett, S. Solomon, P.A. Stott and T. Nozawa (2007) Detection of human influence on twentieth-century precipitation trends. *Nature*, **448**, pp 461-465. doi: 10.1038/nature06025